AN ABSTRACT OF THE DISSERTATION OF

James E. S. Haggerty for the degree of Doctor of Philosophy in Physics presented on June 14, 2018

Title: Amorphous TiO_2: A Thin Film Synthesis Route to Stabilization of Metastable TiO_2 Brookite

Abstract approved:

_____

Janet Tate

Structure-specific synthesis processes are of key importance to the growth of polymorphic functional compounds such as TiO_2, where material properties strongly depend on structure as well as chemistry. The robust growth of the brookite polymorph of TiO_2, a promising photocatalyst, has been difficult in both powder and thin-film forms due to the disparity of reported synthesis techniques, their highly specific nature, and lack of mechanistic understanding. In this work, we report the growth of high-fraction (~95%) brookite thin films prepared by annealing amorphous titania precursor films deposited by pulsed laser deposition. We characterize the crystallization process, eliminating the previously suggested roles of substrate templating and Na helper-ions in driving brookite formation. Instead, we link phase selection directly to film thickness and average deposition rate, offering a novel, generalizable route to brookite growth that does not rely on the presence of extraneous elements or specific lattice-matched substrates. To further explore the growth process of brookite from amorphous precursors, in-situ XRD and in-situ optical microscopy/Raman spectroscopy are used to show that brookite is the first polymorph to form during annealing but that anatase growth is not far behind. Thus, the growth of these two polymorphs are difficult to separate via thermal treatment alone and suggests further that modifications to the amorphous precursor are needed to facilitate brookite formation. Then exploring different PLD parameters that could affect the amorphous precursor, such as average deposition rate and deposition oxygen pressure, we further show the combined

structural and stoichiometric requirements for brookite stabilization. Once crystallized, high-fraction brookite films further exposed to higher annealing temperatures (up to 700°C) show little transformation of brookite regions and no large scale polymorphic transformations. In addition to providing a new synthesis route to brookite thin films, our results take a step towards resolving the problem of phase selection in TiO_2 growth, contributing to the further development of this functional material.

Amorphous TiO_2: A Thin Film Synthesis Route to Stabilization of Metastable TiO_2 Brookite

by
James E.S. Haggerty

A DISSERTATION

submitted to

Oregon State University

in partial fulfillment of
the requirements for the
degree of

Doctor of Philosophy

Presented June 14, 2018
Commencement June 2019

Doctor of Philosophy dissertation of James E.S. Haggerty presented on June 14, 2018

APPROVED:

Major Professor, representing Physics

Head of the Department of Physics

Dean of the Graduate School

I understand that my dissertation will become part of the permanent collection of Oregon State University libraries. My signature below authorizes release of my dissertation to any reader upon request.

James E.S. Haggerty, Author

ACKNOWLEDGEMENTS

All research contained within was funded by the Department of Energy (DOE), in the Energy Frontier Research Center (EFRC) collaboration known as the Center for the Next Generation of Materials by Design: Incorporating Metastability (CNGMD). Within this collaboration I had the distinct pleasure of working with scientist with many different talents and abilities for materials research from around the world and from institutions across the united states including National Renewable Energy Laboratory, Lawrence Berkley National Lab, Harvard, Stanford Synchrotron Radiation Lightsource, Massachusetts Institute of Technology, Colorado School of Mines, and Oregon State University. Since the size of this collaboration includes well over 50 scientists and I cannot thank them all must limit myself to thanking those I interacted with the most.

Laura Schelhas from SLAC, Daniil Kitchaev from MIT, John Mangum from CSM, Wenhao Sun from LBNL, Lauran Garten from NREL are some of the people who had the largest impact on my development as a scientist and as a person. I am grateful to Daniil and Wenhao for their deep understanding of the underlying theory of material systems and their unique perspectives that always led to lively debates. My thanks must further be extended to both Laura and John who in addition to being exceptional materials characterization experts using synchrotron XRD and HRTEM respectively always seem to have smiles on their faces. Then finally I am grateful to Lauren for sharing her extensive technical expertise in thin film synthesis and characterization.

Finally, I would be remiss if I did not recognize the people closest to me throughout constructing this body of work, my advisor Janet Tate and my lab partners Bethany Mathews and Okan Agirseven. Bethany and I joined Janet's lab at roughly the same time and, on top of achieving some very substantial accolades as a scientist, she has been a source of encouragement for me when I needed it the most, something that can never be understated or undervalued. Then lastly but certainly not least, Janet's support and vast network of connections with scientist all over the world has provided me with a diverse and very formative experience that I will never forget.

CONTRIBUTION OF AUTHORS

XRD was performed at SLAC by Laura Schelhas in Michael Toney's group. Electron microscopy was performed at CSM by John Mangum in Brian Gorman's group. DFT calculations were performed at MIT by Daniil Kitchaev, and additional theoretical guidance was provided by Wenhao Sun from LBNL, both in Gerbrand Ceder's group. Initial PLD of films was performed at NREL by Lauren Garten in David Ginley's group.

TABLE OF CONTENTS

Page

1. Introduction 1

1.1. Metastability 1
1.2. The Amorphous State: Accessing Meta-Stable Polymorphs 3

2. TiO_2 Literature Review 6

2.1. Experimentally Known Synthesis Pathways 6
2.2. Theoretical Predictions of TiO_2 Polymorph Energy Ordering 9

3. Materials and Methods 10

3.1. Film Synthesis 10
3.1.1. Thin Film deposition 10
3.1.2. Annealing 11
3.1.3. In-Situ Optical Microscopy/Raman Spectroscopy 11
3.2. Film Characterization 12
3.2.1. Optical Spectroscopy and Hyper-Spectral Mapping 12
3.2.2. Micro-Raman Spectroscopy 14
3.2.3. X-Ray Diffraction 14
3.2.4. Transmission Electron Microscopy 16
3.2.5. Theory 16

4. Results and Discussion 18

4.1. High-fraction brookite films from amorphous precursors [45] 19
4.1.1. Theory 19
4.1.2. Observation of brookite in films on different substrates 21
4.1.3. Film thickness and polymorph fraction 25
4.2. TiO_2 Polymorph Selection 26
4.2.1. Plume Position and Deposition Rate 26
4.2.2. Deposition Oxygen Pressure (pO_2) 31
4.2.3. TiO_2 Thin Film Optical Response: From Spectral to Hyper-Spectral 38
4.3. Brookite Growth, and High Temperature Stability 41
4.3.1. In-Situ Micro-Raman Spectroscopy and Optical Microscopy 41
4.3.2. Post-Anneal Brookite Morphology 47
4.3.3. High Temperature Polymorph Stability 51

TABLE OF CONTENTS (Continued)

5. Conclusion 54

6. Works Cited 56

APPENDICES 61

A1. Crystalline Depositions 62

A2. Optical Band Gap Determination: Toy Model Approach 63

LIST OF FIGURES

Figure Page

Figure 1.1: Classes of metastable materials (shown in color) targeted for theory-driven synthesis in the CNGMD EFRC. 2

Figure 1.2 Sketch of the potential energy surface of solids with different polymorphs corresponding to different PES local minima. [8] 3

Figure 1.3: A schematic Gibbs free energy (G) versus temperature (T) diagram typically used to explain polymorphic systems [9]. 4

Figure 2.1 Crystal structures of TiO_2 rutile (tetragonal, $P4_2/mmm$), brookite (orthorhombic, Pbca) and anatase (tetragonal, $I4_1/amd$) polymorphs. 6

Figure 2.2: Convex hull diagram for the Ti-O material system, focused on the TiO_2 stoichiometry. The blue dots correspond to the different structures predicted by DFT that either exist or are predicted to exist. [39] [40] 9

Figure 3.1 (a) a large 7 cm x 2.5 cm film which is sectioned into 70 5 mm x 5 mm cells each with a thickness variation on the order of 5-20 nm across each cell. (b) thickness map of the film in (a) showing that the color variation in the film is indicative of the film thickness. 10

Figure 3.2 Series of optical images showing the polymorph phase fraction calculation process. (a) is the original x100 microscope image. (b) the region in blue is selected and the number of pixels determined for the brookite, rutile labeled red, and amorphous labeled black. (c) The remainder of the film is labeled green for anatase. The black dots in the original image are considered dust, debris, or PLD spit and typically occur in small amounts such that they are ignored as noise in the measurements as they show no consistent correlation with any given polymorph of TiO_2. 14

Figure 3.3: (a) Plot of the average FWHM of peaks for LaB_6 reference, brookite, anatase, and rutile samples. (b) Williamson-Hall plot for a sample containing both anatase and brookite peaks each individually identified and the best fit linear fit function for each. 15

Figure 4.1 Computed low-temperature free energies of (a) Na_xTiO_2 and (b) $Na_{2y}TiO_{2+y}$ compounds, with Ti-O frameworks constrained to those of known TiO_2 phases, as a representative sample of structure selection in the Na_xTiO_{2+y} chemical space. The dotted lines denote the global thermodynamic equilibrium in each composition space 20

LIST OF FIGURES (Continued)

Figure 4.2: 2D XRD pattern of a TiO_2 film after annealing. The strongest peaks are brookite (121) at Q = 2.166 $Å^{-1}$ and anatase (101) at Q = 1.787 $Å^{-1}$. Brookite (121) has a limited χ range, indicating that brookite crystallites are preferentially oriented. 21

Figure 4.3: (a) XRD patterns of annealed TiO_2 films grown on a-SiO_2 and EXG substrates. The brookite and anatase phases appear in similar proportions in films (58 nm and 52 nm thick respectively) on both substrates. (b) The integrated peak areas for brookite (121) [blue] and anatase (101) [green] on a 65-nm film, grown on EXG, as a function of time and temperature during the anneal indicated by the gray line. Both polymorphs crystallize at ~290°C. 22

Figure 4.4: (a) Optical image of a 65-nm TiO_2 film on EXG glass. Regions marked B yield the Raman spectrum for brookite in (b), while those marked A yield the anatase spectrum in (c). The 2D Raman maps at 319 cm^{-1} (d) and 144 cm^{-1} (e) show that the color variations in the optical image correlate with a particular polymorph. The brookite: anatase ratio in this film is 50:50 and no rutile is observed. The dotted lines in (b) and (c) indicate the wavenumber range over which the Raman intensity maps in (d) and (e), respectively, are acquired. 23

Figure 4.5: HRTEM image of a 50-nm TiO_2 film on EXG glass. The selected area electron diffraction patterns in the insets indicate that the grain on the left is anatase and on the right is brookite. The S-shaped grain boundary is approximately 20 nm wide. 24

Figure 4.6: Elemental EDS maps (a, c) of composition of the TiO_2 film in Fig. 5, and the atomic concentration (b, d) along the indicated line. Plots (a, b) trace the substrate/film interface and plots (c, d) highlight the grain boundary. Na (green) is below the detection limit in the TiO_2 film and accumulates near the film-substrate interface. 24

Figure 4.7: Phase fraction of brookite (blue), rutile (red) and anatase (green) polymorph or amorphous component (gray) in TiO_2 films as a function of thickness. Na-free a-SiO_2 and Si/SiO_2 (circles), low-Na EXG (squares) and high-Na SLS (diamonds) substrates are represented. The uncertainty in thickness is ±5 nm for d < 50 nm and ±3 nm for d > 50 nm. 25

LIST OF FIGURES (Continued)

Figure 4.8: (a) and (b) consist of 3 profiles each of two depositions. (a) is a 1 mTorr pO_2 deposition with max thickness of 70 nm. The thickness profile on top (blue) with brookite percentages labeled and high fraction brookite range within the triangular region. Below the thickness map is a morphology map consisting of x50 microscope images in approximately 5 mm intervals across the sample. The numbers in the bottom row and left most column are cell identifiers used to calibrate positions across multiple systems. The bottom image is the corresponding deposition rate profile with the high fraction brookite region located inside the triangle section. (b) is the same set of images as (a) but for another 1 mTorr pO_2 deposition with max thickness 135 nm. The white rectangle indicates the high brookite fraction section. 26

Figure 4.9: Average deposition rate and film thickness as functions of Raman phase fraction. Colors correspond to blue for brookite, red for rutile, and green for anatase. Size of the bubbles corresponds to the polymorph fraction. Inset is phase fraction as a function of film thickness alone for the same data. 28

Figure 4.10: χ-Integrated 2D synchrotron XRD data acquired with x-ray wavelength $\lambda = 0.9744\, nm$. (a) and (b) XRD spectra of 2 sets of different thickness, 40-50 nm and 60-70 nm respectively, films all deposited with the indicated oxygen pressure. Reference peak locations are indicated by the vertical lines at the bottom of the plot and important polymorph peaks are identified, red rutile (110), blue brookite (210), and green anatase (200). (c) is a cartoon graph of the different polymorphs identified by the XRD as a function of both thickness and deposition oxygen pressure. 31

Figure 4.11: Transmission vs light wavelength across 3 amorphous samples at deposition oxygen pressures 0.1 mTorr (a), 1.0 mTorr (b), and 10 mTorr (c) with the corresponding band gap values as function of thickness. The colored lines (blue for brookite, red for rutile, and green for anatase) in the band gap as a function of thickness plots indicate the theoretically predicted band gap values (dashed) and experimentally determined band gap values (solid) for reference. The plot label in the transmission vs wavelength plots corresponds to the large area deposition cell values described in Figure 3.1. 33

LIST OF FIGURES (Continued)

Figure 4.12: Transmission vs light wavelength across 3 deposition oxygen pressures 0.1 mTorr (a), 1.0 mTorr (b), and 10 mTorr (c) all annealed using the 400°C hold RTA profile. (d)-(f) are the different polymorph band gaps as functions of thickness for films with polymorph fractions greater than 0.6. The sample deposition pressure is indicated by the shapes, diamonds for 0.1 mTorr, circles for 1.0 mTorr, and squares for 10 mTorr. The colored lines (blue for brookite, red for rutile, and green for anatase) in the band gap as a function of thickness plots indicate the theoretically predicted band gap values (dashed) and experimentally determined band gap values (solid) for reference. 34

Figure 4.13: (a) lattice strain vs average particle size as determined from Williamson-Hall plots for films with the highest fractions of each polymorph. (b) lattice strain vs deposition rate and deposition pressure for the same films in (a) where the bubble size indicates the deposition pressure (smallest bubble is 0.1 mTorr, and the largest is 10 mTorr). 36

Figure 4.14: Series of x100 optical microscope images showing the morphology as strain decreases. (a) ($\varepsilon = 0.26\%$). (b) ($\varepsilon = 0.13\%$). (c) ($\varepsilon = 0.09\%$). (d) ($\varepsilon = 0.06\%$). As the strain in the film decreases the number of veins decreases as well suggesting that the veins correlate with the strain. 37

Figure 4.15(a) x50 magnification optical microscope image of a film on Eagle XG glass containing all three polymorph phases labeled R for rutile, A for anatase, and B for brookite. (b), (c), and (d) x40 magnification hyperspectral reflectivity of the same section of film in (a) at light wavelengths, 375 nm, 555 nm, and 765 nm respectively. (e) reflectivity as a function of wavelength for the individual regions identified as rutile, anatase, brookite or amorphous. Also included is a traditional spectral reflectivity spectrum from the same sample close to the same region (as seen by the interference fringe at 400 nm. 38

Figure 4.16: (a) Reflectivity as a function of wavelength showing the shift in interference fringes used to determine film thickness. (b) Transmission, reflection and reflection-corrected transmission of a 60-nm high-brookite-fraction film. (c) Absorption coefficient of the film in (b) with arrows labelling the band gaps obtained if the data are analyzed (insets) as indirect (lower value) or direct gap (higher value). 39

LIST OF FIGURES (Continued)

Figure 4.17: Optical transmission as a function of wavelength of light and optical band gap as a function of film thickness for films deposited with oxygen pressures (a) 0.1 mTorr, (b) 1.0 mTorr, and (c) 10 mTorr. The labels on the transmission plots use the same scheme as that described in Figure 3.1 where 1st number is the cell column and 2nd number is the cell row on a large deposition sample. The theoretically predicted and experimentally determined band gaps for each polymorph are labeled on the band gap plots for reference, and the standard error for the experimental the anatase and rutile band gap is 0.1 eV while the standard error for brookite is 0.2 eV. 40

Figure 4.18: (a), (b), (c), (f), (g), and (h) x50 optical microscope snap shot images of brookite growing during a 400°C anneal. Temperature is displayed on the top left of each image, N is the number of events, and the time corresponds to the time since the appearance of the first events (roughly 15.8 minutes). (d) is the number of sites as a function of time and temperature (black) and the nucleation rate (gray). (e) is the brookite area fraction (black) and the area growth rate (gray).....42

Figure 4.19: (a), (b), (c), (f), and (g) x50 optical microscope snap shot images of brookite growing during a 275°C anneal. Temperature is displayed on the bottom left of each image, and the time corresponds to the time in the top left is the time given in (d). (h) is a x100 magnification microscope image of the same section after cooling to room temperature. (d) is the number of sites(black) and the brookite area fraction (gray) as functions of time. (e) are the in-situ Raman spectra for the amorphous region at 250°C (light gray), a brookite region at 275°C (dark gray) and the same region after cooling (black). The reference spectra for brookite (blue, R050591) and anatase (green, R007058) are obtained from the RRUFF online database. 43

Figure 4.20: In-situ Raman measurements of brookite and anatase. The optical images are all x50 magnification and the red circles are of the fiducial debris used to orient the images for comparison. (a)-(b) Optical image and micro-Raman spectra for the small (~1μm) region inside the white box. (c)-(d) measurement of same spot as (a)-(b) roughly 5 minutes later. (d) shows that the light region inside the white box is large enough to show brookite character as seen by the 246 cm^{-1} and 318 cm^{-1} peaks. (e)-(f) Optical image and micro-Raman spectra for a spot between the two brookite regions. (f) shows the region in the white box is amorphous, especially when compared with (b) around 150 cm^{-1}. (g)-(h) Optical image and micro-Raman spectra for a spot close to the one in (e) about 1 hour later after the brookite regions are approaching merging, and still between the two brookite regions. (h) shows the Raman spectrum for the region in the white box in (g) indicating an anatase structure as seen by the peak at 150 cm^{-1} combined with the peak at 400 cm^{-1}. The peaks around 490 cm^{-1}, 600 cm^{-1}, and 800 cm^{-1} are all from the a-SiO_2 substrate.....44

LIST OF FIGURES (Continued)

Figure 4.21: Raman Spectral evolution of amorphous to brookite transition. Red circles indicate fiducial debris for reference and white boxes indicate laser position and size. 46

Figure 4.22: (a), (b), and (c) post-anneal x100 microscope images of samples annealed in-situ up to the given maximum temperature. (d) point-Raman spectra of the spot inside the black circle in (a), (b), and (c). The white arrow in the images indicates the laser polarization, while the black arrow indicates the major growth direction for the brookite region measured. 47

Figure 4.23: 2D Micro-Raman map of 400°C annealed sample. (a) x100 microscope image of brookite region containing multiple brookite veins. The 3 most prominent veins are labeled 1-3 for reference in the Raman maps. (b), (c), (d), and (e) are intensity maps of the Raman spectra taken across the image in (a). Each Raman intensity map is centered on the given polymorph peak and the vein-like structure can be seen in each map as a decrease in Raman intensity. 48

Figure 4.24: (a) x100 optical microscope image of a 400°C annealed sample. (b) 2D Micro-Raman map with the intensity for the brookite 318 cm^{-1} peak ±5 cm^{-1}. The bright yellow regions indicate where the brookite sections are within the optical microscope image in (a). (c) AFM map of the same region in (a) and (b). Yellow arrows indicate brookite wisps, white arrows indicate veins, and the sections labeled B are identified by the Raman intensity map as brookite. 50

Figure 4.25: 39 nm thick high fraction brookite film initially annealed with the 400°C hold RTA profile(a), then annealed in the oven at 600°C for 15 minutes, 1 hour, and lastly 24 hours (b) all at ambient atmosphere. (a) and (b) are both x100 magnification images. The black and white boxes in (b) indicate the position of the laser during two of the measurements. (c) the Raman spectra of the same spot measured after each anneal (d) is the same data as (c) but zoomed into the brookite 318 cm^{-1} peak. (e) the Raman spectra centered on the anatase 394 cm^{-1} peak. The shift in these peaks as a function of annealing time is within the experimental uncertainty (± 3 cm^{-1}) for this measurement. 51

Figure 4.26: 43 nm thick high fraction brookite film initially annealed with the 400°C slow RTA profile, then annealed in the oven at 700°C for 15 minutes (a), then 24 hours (b) at ambient atmosphere. (a) and (b) are both x100 magnification images. (c) the Raman spectra of similar regions measured after the all anneals. (d) is the same data as (c) but zoomed into the brookite 318 cm^{-1} peak. The shift in these peaks as a function of annealing time is within the experimental uncertainty (± 3 cm^{-1}) for this measurement. 52

LIST OF TABLES

Table Page

Table 2.1 Formation mechanisms reported for some metastable TiO_2 polymorphs. All polymorphs transform to rutile above 600 - 700°C. 7

Table 2.2 PVD of phase pure brookite reported in the literature 8

1. Introduction

1.1. Metastability

In this work, we report a simple, substrate agnostic synthesis route that produces a high fraction of the TiO_2 brookite phase in a thin film by pulsed laser deposition (PLD) of amorphous TiO_2 and subsequent annealing. Modifications of the amorphous matrix prior to annealing was shown in other material systems, such as VO_2 [1], as a synthesis route to high energy metastable polymorphs. We characterize the resulting films through 2D synchrotron X-ray diffraction (XRD), 2D micro-Raman spectroscopy, high resolution transmission electron microscopy (HRTEM), energy dispersive X-ray spectroscopy (EDS) and first-principles calculations to confirm the presence of brookite and discuss the possible mechanisms leading to its formation.

We produce thin films with more than 90% brookite, investigate the in-situ[1] interplay of brookite with the more common rutile and anatase polymorphs as they grow, and eliminate several reaction mechanisms previously proposed based on sol-gel and hydrothermal growth results. Specifically, we investigate the proposed role of Na in promoting brookite growth as it migrates into the growing film from the substrate [2] [3] [4], and demonstrate that contrary to previous reports [5] [6], brookite growth does not depend on the presence of Na. Instead, the nucleation and growth of brookite appears to rely on processing and structural properties such as film thickness, average deposition rate, and deposition oxygen pressure.

Through the investigation of brookite formation, some interesting observations are made that warrant additional documentation. For instance, while crystallizing, interesting morphological features manifest including structures we name veins and wisps. Additionally, transmission and reflection spectroscopy are used to document the band gap dependence on film thickness before and after annealing, showing that even before the films are annealed the amorphous matrix show indications of the different polymorphs. Finally, we document the thermal stability of high-fraction brookite films by annealing them at higher temperatures (up to 700°C), showing a distinct lack of transformation to the

[1] References to in-situ in this study all pertain to the monitoring of the crystallization process from amorphous TiO_2 to crystalline thin films.

ground state rutile structure. The vast array of characterization techniques used, and analysis performed would not be possible without the large collaborative effort of the Center for the Next Generation of Materials by Design: Incorporating Metastability (CNGMD) and their push toward theory-guided synthesis.

Theory-guided synthesis is the idea that the tools available to theorist today may be powerful enough to reverse the order by which scientific understanding is obtained. In previous generations, scientific advancement came about through experimental discovery followed by theoretical understanding. For example, in 1785 William Morgan presented a paper to the Royal Society of London describing "the effects of passing currents through evacuated glass tubes" [7], an experimental discovery. More than 100 years later, in 1895, German professor Wilhelm Röntgen studied these effects and attributing them to a "new kind of ray" (theoretical explanation) giving name to what is known today as the x-ray [7]. Theory guided synthesis seeks to show, with the computational power available today, that scientific knowledge might be obtained by predicting interesting material properties with theory and using them to direct experimental efforts.

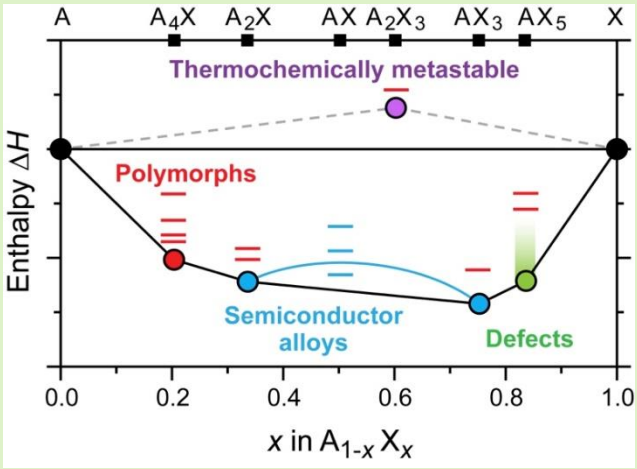

Figure 1.1: Classes of metastable materials (shown in color) targeted for theory-driven synthesis in the CNGMD EFRC.

One of the things standing in the way of creating a more clear and consistent application of theory guided synthesis is metastability. The CNGMD effort identifies multiple metastable pathways in which a clearer theoretical understanding is needed: defects, disorder, and interfaces, semiconductor alloys, and polymorphism. Figure 1.1 is known as a convex hull diagram and represents each of these metastable states as large variations in material composition (semiconductor alloys), large variations in crystal structure (polymorphism), or as small deviations in stoichiometry and/or structure (defects or disorder). As defects, disorder, and interfaces

and semiconductor alloys are outside the scope of this research, the work here in focuses on the polymorphic aspect of metastability.

1.2. The Amorphous State: Accessing Metastable Polymorphs

Polymorphism corresponds to different structures that a material can assume without changing its elemental composition. It is represented by the horizontal bars stacked in columns above the dots in Figure 1.1. By far the most common method for describing the polymorph energy landscape (or energetic ordering) is by looking at the formation energies for each polymorph relative to the ground state structure [8]. Stevanović [8] argues that this method is only a minor component in determining the realizability of a given polymorph. The other two aspects of polymorphism needed to describe these complex transformations are the energy barrier inhibiting the material from transforming and the volume of the polymorph energy well. The latter aspect is the most important for determining the likelihood of synthesizing the desired polymorph, as it relates directly to the likelihood of the polymorph forming in the first place.

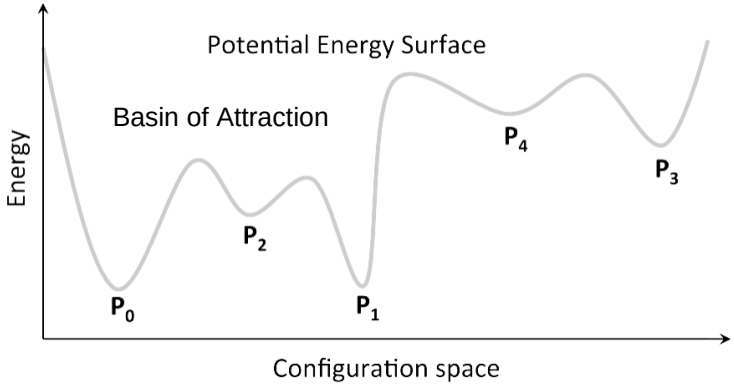

Figure 1.2 Sketch of the potential energy surface of solids with different polymorphs corresponding to different PES local minima. *[8]*

As described by Stevanović Figure 1.2 is an example of a possible potential energy surface (PES) for a polymorphic system. The horizontal axis, or configuration space corresponds to whatever control parameter(s) is needed to form a specific structure. Whether the configuration space is thermal treatment or stoichiometric variation or pressure treatment or dopants or some other control parameter, the result is the same a change in the materials internal energy. As shown in Figure 1.2, a material system contains different types of equilibria (the polymorphs, P_i, and the global minimum, or ground state, P_0). The polymorphs represent the accessible states in a materials system and, depending on the volume (area in this 2D representation) of the potential energy well, can be very difficult to transform into one another once stabilized (except for the ground state structure which all polymorphs transform into eventually). Amorphous states, on the other hand, are states a material can assume like the polymorphs P_3 and

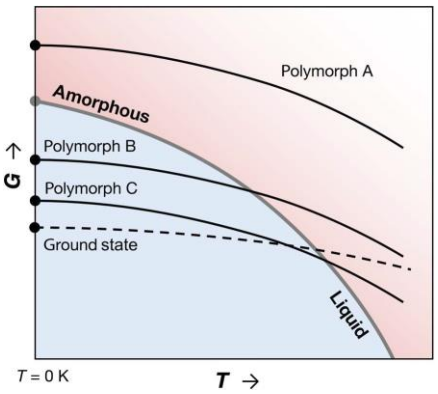

Figure 1.3: A schematic Gibbs free energy (G) versus temperature (T) diagram typically used to explain polymorphic systems [9].

P_4, higher in energy than the other polymorphs and with lower energy barriers to transformation. The ground state structure is defined as the polymorphic structure with the lowest energy and the largest volume energy well such as the polymorph P_0. This description provides an excellent view of the polymorph energy landscape but provides little insight into how polymorphs can be transformed from one structure to another or even how the amorphous phases can be used to synthesize higher energy polymorphs. To understand how amorphous depositions can aid in synthesizing higher energy polymorphs, we must turn our attention to the "thermodynamic limit for synthesizability" [9].

The thermodynamic limit to synthesizability was determined to be the high energy amorphous structures within a material system [9]. This suggests that while theory may predict numerous possible crystal structure available within a given stoichiometry, the amorphous states provide the upper limit for crystal structure stability. Thus, a crystal structure that is higher in energy than the amorphous phase is not likely to be synthesized. Furthermore, of interest to the TiO_2 system, is the concept that higher energy polymorphs can be accessed "downhill" in the energy scale from the amorphous state.

Consider Figure 1.3, a Gibbs free energy diagram for a general polymorphic system. Using temperature as our control parameter we see that a system in the ground state structure can require a considerable increase in temperature before transforming into the next most stable polymorph (C)[2]. Since the transformation crossover from the ground state to polymorph C is so close to the liquid transformation, the window of synthesis may be very small. Furthermore, if we wanted to synthesize polymorph B from the ground state, the material would melt before transforming, making it all but impossible to synthesize. However, if instead we were able to synthesize our material in an amorphous state, through thermal treatment we should find that polymorph B forms at a lower

[2] By following the dotted line from left to right until it intersects the solid line for polymorph C.

temperature than even the ground state structure. This explains the “downhill” access of higher energy metastable polymorphs. The aim of this work in the coming chapters is then to elaborate on the subtleties of brookite stabilization from amorphous precursors in the TiO_2 material system.

In the coming chapters we will discuss the stability window for the three most common polymorphs in the TiO_2 system: rutile, anatase, and brookite. This research focuses specifically on PLD of amorphous TiO_2 combined with thermal treatment to form the metastable brookite phase. We begin by first discussing the current state of brookite synthesis within the physical vapor deposition (PVD) community as it relates to the hydrothermal synthesis communities known recipes for brookite formation. Within the literature review, we also discuss the Ti-O convex hull, band structures of the three polymorphs, and their optical properties. After the literature review, we detail the materials and methods used to characterize the PLD thin films which include multiple annealing systems, transmission/reflection spectroscopy, hyperspectral reflectivity mapping, 2D synchrotron XRD, HRTEM, EDS, as well as in-situ characterization techniques such as XRD and optical microscopy/Raman spectroscopy. Then we present the results from our investigation including the deposition range required for brookite synthesis such as film thickness/deposition rate dependence, and a strong dependence on oxygen pressure during deposition. Furthermore, the in-situ annealing study shows that while temperatures as low as 250°C are sufficient to nucleate brookite from amorphous precursors, ultimately different thermal treatments produce minimal difference in the final crystalline composition of the films, suggesting that the composition of the amorphous precursor can be used to control the final crystalline product.

2. TiO_2 Literature Review

2.1. Experimentally Known Synthesis Pathways

TiO_2 can form in many structures, the most prominent of which are the naturally-occurring rutile, anatase and brookite polymorphs depicted in Figure 2.1, although many other synthetically prepared structures have been reported [10] [11]. Rutile, the ground state, and anatase are by far the most common and find many applications [12] [13], from paint pigments to transparent conductors and photocatalysts. Brookite is seeing renewed interest [14] [15] [16], with a rutile/brookite mixture serving as effective photocatalysts and outperforming Degussa P25 (an anatase/rutile mixture commonly used) at degrading both rhodamine B and methyl orange. Furthermore, through surface engineering, brookite can become either oxidative or reductive [17] depending on the exposed surface ((201) or (210) respectively), adding versatility as a catalyst. However, the synthesis of high-quality brookite has proven much more difficult than that of rutile and anatase, motivating us to study its formation in the form of a functionally-relevant thin film.

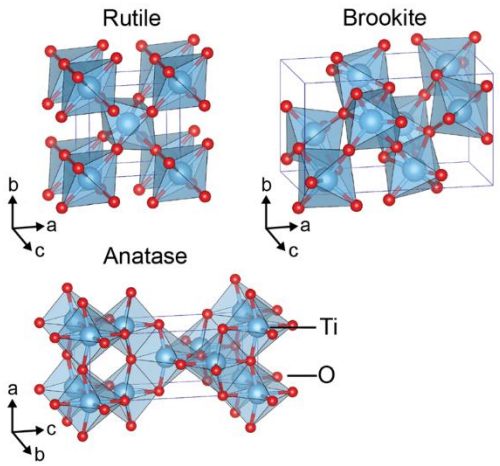

Figure 2.1 Crystal structures of TiO_2 rutile (tetragonal, $P4_2/mmm$), brookite (orthorhombic, Pbca) and anatase (tetragonal, $I4_1/amd$) polymorphs.

Designing a synthesis route to a metastable phase such as brookite requires the knowledge of both equilibrium and non-equilibrium reactions that could occur [18]. Although phase diagrams of the bulk Ti-O system under standard conditions are established, phase selection during synthesis is not merely a matter of bulk equilibrium thermodynamics, as evidenced by the ubiquity of metastable, non-equilibrium synthesis products, which include anatase and brookite. As reported in similar ionic systems, synthesis routes to various stable and metastable phases can be driven by finite-size effects [19], nucleation kinetics [20] [21], bulk and surface off-stoichiometry [22] [23] and others [24] [25]. Table 2.1 lists several proposed stabilization mechanisms for the common TiO_2 polymorphs, as well as the conditions driving their transformations. In the case of brookite, it appears that the most efficient reactions leading to the bulk material are crystallization by sol-gel and hydrothermal techniques in the presence of Na or some

other alkali ion spectators [5] [6]. However, there is no established mechanistic understanding of these synthesis routes. Moving further beyond bulk synthesis, the growth of materials as thin-films opens the door to high-energy synthesis methods such as sputtering and PLD. Although thin films of brookite have been obtained by PVD on lattice-matched substrates [26] [27] [28] [29] (Table 2.2), the non-equilibrium growth of high-purity brookite on amorphous substrates has been largely unexplored.

Table 2.1 Formation mechanisms reported for some metastable TiO_2 polymorphs. All polymorphs transform to rutile above 600 - 700°C.

TiO_2 Polymorph/Transformation	Stabilization/Formation Mechanism
Anatase	Smaller crystal sizes and lower pressure [30].
Anatase→Rutile	Growth post-nucleation to a large crystal size, reconstructive process [12]
Anatase→Baddeleyite	Small crystallite sizes under high pressures (24)
Anatase→α-PbO_2	Large nanocrystals to macroscopic single crystals under high pressures (24)
Anatase→Brookite	Controlled size in the tens of nanometers regime and the presence of surfactants [19] [31] [32] Twinning on anatase {112} facets [33]
Brookite	Helper ions such as NaOH [5], $C_2H_2O_4$+polymer [34], pH during hydrothermal reaction [17], or Cl^- ions [35] during either solution or hydrothermal synthesis. - Intermediate crystallite sizes [19]

The lack of a clear and consistent mechanistic understanding of brookite growth explains the wide variety of hydrothermal and sol-gel synthesis approaches found in literature [12] [13]. Some reports find that high concentrations of NaOH lead to the best brookite samples [36], while others use a combination of inorganic and organic precursors to produce phase pure brookite [34], and others report pure brookite based on a delicate balance between Cl^- ion concentration, pH, and the necessity of the $[Ti(OH)_2(Cl)_2(OH_2)_2]^0$ salt as a brookite precursor [35]. One common thread between these recipes is the use of some ionic complexing agent (Na^+, $C_2O_4^{2-}$, or Cl^-) to favor the structural selection of brookite in large quantities. However, PVD processes inspired by the proposed growth mechanisms do not consistently lead to the same results [2].

One of the reasons for the discrepancies between solution-based and vapor-based results, and the difficulty of synthesizing brookite via PVD, could be the delicate balance of thermodynamic forces favoring each polymorph [19], which are difficult to transfer precisely between growth techniques. Another possibility is that helper species present during hydrothermal or sol-gel growth (e.g. Na^{+}, $C_2O_4^{2-}$, Cl^{-}) are not typically used during PVD growth, limiting the accessible pathways to the ones without these helper species. As a result, to date synthesis of pure brookite by PVD has relied on highly specific stabilization mechanisms, namely substrate lattice-matching, to produce any thickness of thin-film brookite. The first study to produce brookite via PVD [29] relied on plasma-enhanced chemical vapor deposition (PECVD) with titanium tetra-isopropoxide (a common precursor used in TiO_2 hydrothermal growth) vapor on (100)-oriented silicon substrates. Other works [26] [28] have reported lattice-matched brookite growth on (110) yttria-stabilized zirconia (YSZ) by plasma-enhanced atomic layer deposition (PEALD) and metal-organic chemical vapor deposition (MOCVD), reporting an in-plane orientation of $[001]_{brookite}//[001]_{YSZ}$ and an out-of-plane orientation of $[120]_{brookite}//[110]$. In one case, a brookite nanorod film was reported [27] grown by matrix-assisted pulsed laser evaporation (MAPLE), using a target made from a suspension of solution-synthesized brookite nanorods frozen in liquid nitrogen, onto (100) Si substrates. Furthermore, of the brookite formation studies on amorphous glass substrates [37] [38], the highest brookite fraction reported to date is 45 ± 15% [37] with the remaining film composed of rutile and anatase. Thus, despite the relative abundance of synthesis routes yielding brookite from solution,

Table 2.2 PVD of phase pure brookite reported in the literature

PVD Method	Substrate	Thickness (nm)
PEALD [26]	(110) YSZ	~80
MAPLE [27]	(100) Si	~50
PECVD [28]	(100) Si	Unknown
MOCVD [29]	(110) YSZ	60

there remains no established mechanism reported for the formation of high-fraction brookite on general, non-lattice-matched or amorphous substrates.

2.2. Theoretical Predictions of TiO_2 Polymorph Energy Ordering

Using computational approaches, the predictions for both polymorph energy ordering and stability can be complicated. As mentioned earlier, the most common method for determining polymorph ordering is via DFT calculations and the formation energy associated with a specific crystal structure, carried out assuming a temperature of zero kelvin. Figure 2.2 is the convex hull diagram for the Ti-O system focusing on the TiO_2 stoichiometry from the materialsproject.org [39] [40].

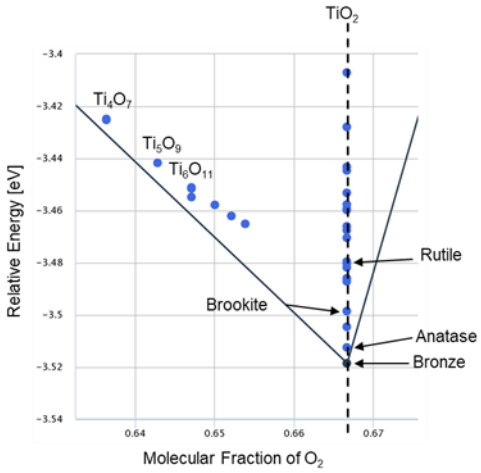

Figure 2.2: Convex hull diagram for the Ti-O material system, focused on the TiO_2 stoichiometry. The blue dots correspond to the different structures predicted by DFT that either exist or are predicted to exist. [39] [40]

The first interesting feature observed in Figure 2.2 is that the ground state structure is not rutile, which is almost universally accepted as the ground state [41] [15] [36] [11] [31] [14] [42] by experimentalists. Instead the ground state structure is predicted to be TiO_2 (B) or bronze which is a monoclinic polymorph that can be stabilized via Na intercalation [2], the process proposed to stabilize brookite investigated in this work.

The next interesting feature in Figure 2.2 is that there are numerous polymorphs predicted to exist within the TiO_2 system, some of which have been experimentally verified and reported within the International Crystal Diffraction Database (ICDD). If we focus our attention only on the three most common polymorphs, rutile is predicted to be the least stable, and apart from bronze being the predicted ground state structure, the energy ordering of anatase, brookite, then rutile (increasing order) agrees with the more accurate Quantum Monte Carlo calculations [43] at zero kelvin. This ordering, however, is in complete disagreement with calorimetry experiments [19] which show that rutile is the most stable polymorph, followed by brookite and then anatase.

3. Materials and Methods

3.1. Film Synthesis

3.1.1. Thin Film deposition

Using PLD, we deposit amorphous TiO_2 films on Corning Eagle XG glass (EXG, MTI corporation), soda-lime silicate microscope slides (SLS, Corning 0215), fused quartz (a-SiO_2, GM associates), and p-type silicon with a 100-nm-thick thermal oxide (MTI corporation). According to the specification sheets, EXG glass has 0.1 wt. % alkali content, SLS has 14% Na_2O and the fused quartz and p-Si substrates are Na-free. Before deposition, substrates are cleaned with a 1% solution of Liqui-Nox (Cole-Palmer)/deionized water and rinsed in deionized water followed by five-minute ultrasound baths in acetone and then in isopropyl alcohol. Substrates are then dried with compressed nitrogen and stored in a warming oven at 120°C in ambient atmosphere, until being transferred to the vacuum chamber for deposition.

The films are deposited at room temperature in a vacuum chamber with base pressure near 5 x 10^{-7} Torr, purged with ultra-high purity oxygen for five minutes, and then held at a constant O_2 pressure (0.1, 0.5, 1.0, 5.0, or 10 mTorr) during deposition. Substrates are typically 2 cm x 2.5 cm and as large as 7 cm x 2.5 cm, and are held stationary at a target-to-substrate distance of 12 cm. An example of a large substrate deposition is shown in Figure 3.1(a), where the color variation across the film is due to the variation in the film thickness and the resultant interference response. The thickness profile for the film in Figure 3.1(a) is shown in Figure 3.1(b). This distance produces a

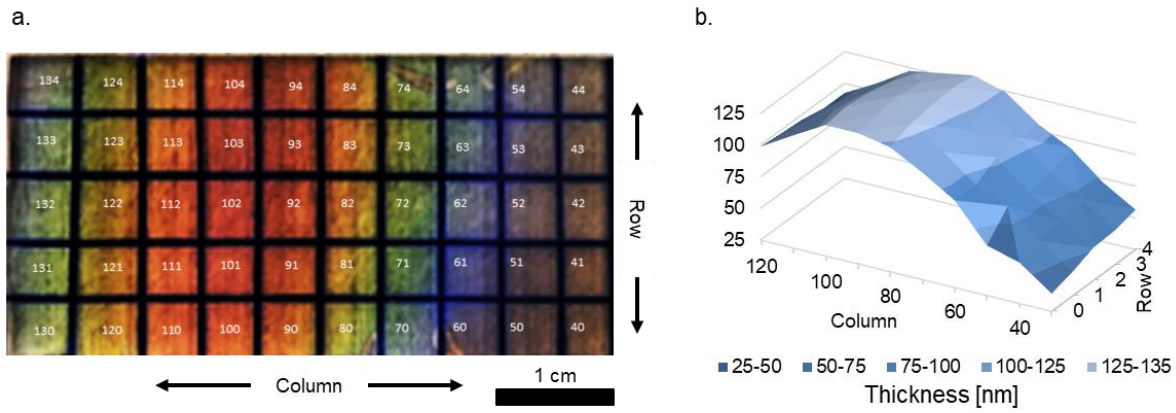

Figure 3.1 (a) a large 7 cm x 2.5 cm film which is sectioned into 70 5 mm x 5 mm cells each with a thickness variation on the order of 5-20 nm across each cell. (b) thickness map of the film in (a) showing that the color variation in the film is indicative of the film thickness.

thickness variation of about 30% across an individual sample, which is useful to investigate the polymorph fraction as a function of thickness. The ceramic target (99.998% TiO_2, Materion) is rotated during deposition to obtain uniform ablation. The output energy from the Lambda Physik KrF excimer laser (λ = 248 nm, ~ 10ns pulse duration, and 10 Hz repetition rate) is typically 150 mJ. The laser energy on the target is 60 mJ giving a laser fluence of 0.54 Jcm^{-2}. The loss of 60% of the laser energy is partially due to the high optical absorption of TiO_2 at 248 nm and has been measured to increase as high as 90% loss as more TiO_2 is deposited on the laser entrance window. To ensure repeatability, we deposit films in two different chambers at NREL and OSU using similar deposition conditions. The substrates are large enough that they can be cleaved into as many as 70 sub-samples so that the same amorphous precursor can be processed or analyzed in different ways.

3.1.2. Annealing

To investigate the effects of different annealing rates and temperatures, rapid thermal annealing is performed in two different ways. In the first method, films are placed on a Si wafer and annealed in an AET Thermal RX Series Rapid Thermal Processing system under flowing N_2 with a flow rate of approximately 10 L min^{-1}. This profile involves a 10 min N_2 purge, 54°C /min ramp up to 340°C, immediately followed by a 30°C /min ramp to 400°C which is then held constant for 3 minutes. Since evacuating the chamber prior to annealing is not an option in this system, there is the additional possibility of atmospheric oxygen affecting the anneal. Then the system is cooled to room temperature (~10 minutes). In the second method, annealing is performed under ambient atmosphere in a Thermolyne Type 4800 oven, pre-heated to a maximum temperature (600°C or 700°C). Once the oven's temperature is stabilized for 15 minutes, samples are placed in the oven for 24 hours and then removed to room temperature to cool.

3.1.3. In-Situ Optical Microscopy/Raman Spectroscopy

During investigation of the growth of brookite crystals from the amorphous thin-film precursors, in-situ optical/Raman spectroscopy is utilized. Since the three different polymorphs are identifiable based on visual contrast [44], the growth of brookite seeds is observable via an optical microscope while annealing. A long working distance x50 microscope objective is attached to the microscope to

avoid damaging the optics at high temperatures. A Linkam THMS600 heating stage is coupled with the micro-Raman system described in Section 3.2.2. Samples are placed in an enclosed container, flushed with N_2 for 5 minutes prior to heating and N_2 continues to flow at 10 LPM for the duration of the anneal. 20°C/min and 150°C/min ramp rates are used to heat the samples up to 275°C, 340°C, and 400°C. Samples are held at their maximum temperature for 5 minutes to 2 hours depending on the observed structures and the number of high temperature Raman spectra needed to characterize each section. A video of the entire annealing process is recorded via OBS studio software by recording a video of the computer monitor. This video is then analyzed to obtain growth rates and nucleation rates for the crystalline regions as they appear.

Growth rates and nucleation rates are computed using VSDC Free Video Editor, and ImageJ. The video is edited (contrast and brightness are adjusted to improve polymorph identification) and cropped. Nucleation rates are determined by first counting the number of visible brookite sites, chosen by following brookite regions backward to their first appearance in time, until all sites are accounted for based on the final structure of the film. Then, assuming each nucleation site is the result of a single nucleation event, the nucleation rate is calculated using a numerical symmetric difference quotient derivative. Next, still images at relevant time intervals, chosen based on the length of the anneal, are exported for further analysis using ImageJ. Within the exported images, 10 nucleation sites are chosen to follow based on their position in the image and their orientation to other sites nearby. The perimeter of each site at each time is then traced using ImageJ and the defined shape is fit with an ellipse to determine major and minor axis lengths in pixels. The pixels are then converted to micrometers and the growth rate determined using a symmetric difference quotient derivative.

3.2. Film Characterization

3.2.1. Optical Spectroscopy and Hyperspectral Mapping

Two different optical spectrometers are used to collect transmission and reflection spectra. First, since some of the samples are rather large they must be divided into smaller sections for consistency of analysis across multiple measuring systems. Each of the 3.5 cm x 2.5 cm samples are divided into roughly 5 mm x 5 mm subsections, resulting in ~35 regions per sample for analysis. To establish a

thickness profile for these samples, transmission in each region is measured in the wavelength range of 200-1000 nm using an Ocean Optics Fiber optic spectrometer consisting of an HR4000 (3648 element Si CCD array) spectrometer and a DH-2000-BAL (deuterium and halogen balanced spectra) lamp. To confirm the thickness and band gap values, select sections are remeasured in both transmission and reflection using a UV-enhanced xenon lamp combined with a grating spectrometer with a double monochromator and single element silicon detector in the wavelength range 200-800 nm.

Due to the contrast in the index of refraction between the glass substrates and TiO_2, thin film interference fringes are observed in the optical spectra. Optical absorption, film thickness, index of refraction, and band gap energy are all determined using these interference fringes as guides. The optical properties for films, for which only transmission data are acquired, are determined using the SCOUT optical data processing software package. The model chosen to fit optical data for TiO_2 includes as parameters: film thickness, index of refraction ($n^2 \approx A + B\lambda^2/(\lambda^2 - IO^2)$), the OJL2 model for interband transition [45] (gap energy, gap strength, gamma, and decay), and a constant imaginary component to the dielectric function. The index of refraction model used approximates the Sellmeier function, which works well for modeling the dispersion relation for transparent media. The OJL2 model [45] is used for the optical band gap and was developed to describe the band gap of amorphous silicon.

To further emphasize the multi-polymorph nature of these thin films, hyperspectral mapping is performed in Dr. Matt Graham's lab using a double monochromator channeled into a microscope via a fiber optic cable. This allows the light source to be varied in 1 nm steps and the spatial reflectivity is measured using a reflective x40 magnification objective and a ProEM back illuminated electron multiplying (512 x 512 pixel) CCD array to record the microscope image. The result is a stacked .tiff file which is analyzed in ImageJ where each polymorph perimeter is defined, and the average region intensity calculated for each wavelength. This allows the reflectivity of each polymorph in the microscope image to be plotted individually. Where a typical spectral measurement would only give the average response for all the polymorphs in a 1 mm^2 region, the hyperspectral map offers spatial resolution of the reflectivity within an approximately 1 μm^2 region.

3.2.2. Micro-Raman Spectroscopy

Micro-Raman spectroscopy is performed using a Horiba Jobin-Yvon LabRam800 with 532-nm laser excitation and a beam of about 1 μm in diameter. Data are processed using the LabSpec 6.0 software suite. Each polymorph optical region is measured at a single point in the wavenumber range 50 – 850 cm^{-1} using a 1200-lines per mm diffraction grating, and a confocal hole diameter of 200 μm. A high pass filter designed to filter out the Rayleigh scattered light, which is scattered at the same wavelength (532 nm) as the incident laser light, is employed so the weakly scattered Raman light can be more easily distinguished. After background subtraction (substrate influence plus residual), peaks are fit with Gaussian functions to identify peak position, amplitude, width, and compared to reference spectra reported in the RRUFF database [46] for polymorph identification.

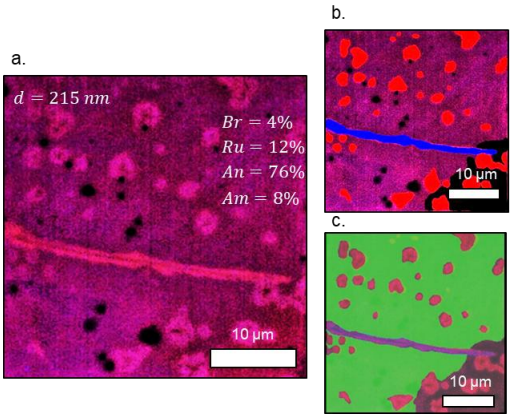

Figure 3.2 Series of optical images showing the polymorph phase fraction calculation process. (a) is the original x100 microscope image. (b) the region in blue is selected and the number of pixels determined for the brookite, rutile labeled red, and amorphous labeled black. (c) The remainder of the film is labeled green for anatase. The black dots in the original image are considered dust, debris, or PLD spit and typically occur in small amounts such that they are ignored as noise in the measurements as they show no consistent correlation with any given polymorph of TiO_2.

2D micro-Raman mapping is performed by inserting a motorized mirror in the laser beam line allowing the laser to be positioned and scanned across the sample. Polymorph fraction is calculated from the area in such 2D Raman maps or from corresponding optical images over an area of approximately 150 μm x 150 μm. An example of the process of polymorph phase fraction calculation is given in Figure 3.2.

3.2.3. X-Ray Diffraction

XRD is performed by staff scientist at the Stanford Synchrotron Radiation Lightsource (SSRL) using Beamline 11-3 with an X-ray energy of 12.7 keV. Two-dimensional scattering data are collected using a Rayonex charge-coupled device and in a grazing incidence geometry with the x-ray beam held at an incident angle of 3°. Images are calibrated using a LaB_6 standard and integrated between $10° < \chi < 170°$ (χ is the polar angle) using GSAS-II [47]. The background due to the amorphous substrate is subtracted using the PDXL software package. Peak positions are manually picked within

the PDXL software package which uses a least-squares algorithm to refine, the peak position, peak intensity, and FWHM. These parameters are all then used to search the International Crystal Diffraction Database (ICDD) for the material that best fits the data, allowing phase identification. Once the peaks are assigned to a polymorph the peak position and FWHM are used to construct a Williamson-Hall [48] plot to determine average crystallite size and average lattice strain.

Before performing the Williamson-Hall analysis of the thin film, a base line for the strain must be set. Figure 3.3(a) is a plot of the FWHM for the calibration standard LaB_6 and three films which are identified as containing a majority phase of the indicated polymorph (red for rutile, blue for brookite, and green for anatase). This plot shows that for the integrated 2D XRD data the calibration standard shows the least amount of peak broadening, indicating that most of the broadening in the TiO_2 thin

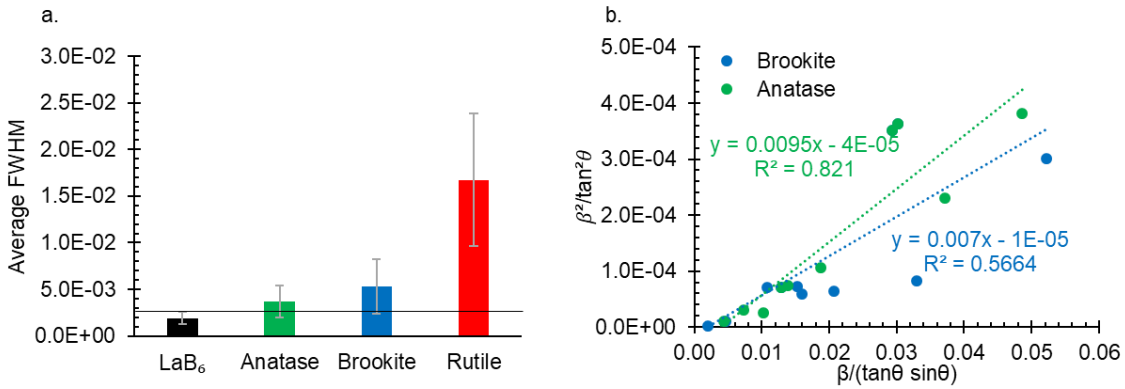

Figure 3.3: (a) Plot of the average FWHM of peaks for LaB_6 reference, brookite, anatase, and rutile samples. (b) Williamson-Hall plot for a sample containing both anatase and brookite peaks each individually identified and the best fit linear fit function for each.

films is due to size or strain effects.

The Williamson-Hall [48] method assumes that both the strain and size effects on the peak broadening (β) is additive.

$$\beta_{\text{total}} = \beta_{\text{size}} + \beta_{\text{strain}} \qquad (3\text{-}1)$$

The peak broadening due to particle size effects is given by the Scherrer equation $\beta_{\text{size}} = K\lambda/L\cos\theta_{hkl}$, where $K = 0.9$ is a dimensionless constant that varies with the shape of the crystallite, $\lambda = 0.9744\ nm$ is the x-ray wavelength, L is the average particle size, and θ_{hkl} is the Bragg angle. The effect of instrumental broadening is accounted for using $\beta_{\text{total}} = \beta_{sample} - \langle\beta_{\text{inst}}\rangle$, with $\langle\beta_{\text{inst}}\rangle =$

0.002 with a standard deviation $\sigma = 0.0006$. Then the peak broadening due to non-uniform strain is derived from differentiating Bragg's Law

$$\beta_{strain} = \Delta 2\theta = 2\frac{\Delta d}{d}\tan\theta \qquad (3\text{-}2)$$

and then assuming equal contributions from tensile and compressive strain we multiply by 2 to obtain the maximum strain, $\beta_{\text{strain}} = 4\varepsilon\tan\theta$ where $\varepsilon = \Delta d/d$ is the average percent lattice strain. With a bit of algebraic manipulation, it can be shown that,

$$\frac{\beta_{total}^2}{\tan^2\theta} = (4\varepsilon)^2 + \frac{K\lambda}{L}\frac{\beta_{total}}{\tan\theta\sin\theta} \qquad (3\text{-}3)$$

which is a linear when $\beta_{total}^2/\tan^2\theta$ is plotted as a function of $\beta_{total}/\tan\theta\sin\theta$. The slope of the linearized plot is then associated with the average particle size, and the intercept is associated with the average strain. An example plot of this type of linearization is given in Figure 3.3(b) for a sample containing peaks associated with both anatase and brookite.

3.2.4. Transmission Electron Microscopy

TEM micrographs are acquired by scientists at the Colorado School of Mines with an FEI Co. Talos F200X transmission electron microscope with scanning capabilities operating at an accelerating voltage of 200 keV. Specimens for TEM are prepared from deposited films via *in-situ* focused ion beam lift-out methods [49] using an FEI Co. Helios Nanolab 600i SEM/FIB DualBeam workstation. Specimens are ion milled at 2 keV and 77 pA to remove Ga ion beam damage and achieve a final thickness of approximately 80 nm. Structural characterization is conducted by acquiring selected area electron diffraction (SAED) patterns on an FEI Co. Ceta 16M pixel CMOS camera at a camera length of 410 mm. Platinum from the FIB is used to calibrate the camera constant, allowing SAED reflections to be accurately measured and indexed. Chemical mapping is performed in the TEM using the Super-X energy-dispersive X-ray spectroscopy (EDS) system equipped with four windowless silicon drift detectors, allowing for high count rates and chemical sensitivity to 1 atomic percent.

3.2.5. Theory

To model the thermodynamics of possible growth mechanisms, theorists at the Massachusetts Institute of Technology use density functional theory (DFT) as implemented in the Vienna Ab-Initio

Simulation Package (VASP) [50], relying on the SCAN exchange-correlation functional [21], projector augmented wave method [51], and a reciprocal space discretization of 25 $Å^{-1}$. We choose the SCAN functional as it was recently demonstrated to generally produce accurate results in phase selection among polymorphs in similar systems [22], and accurate formation energies for titanium oxides in our own benchmarking.

We evaluate the effect of sodium incorporation into titania polymorphs (i) as accompanied by reduction of Ti, and (ii) as a neutral Na_2O defect. We enumerate likely phases in the TiO_2-$NaTiO_2$ and TiO_2-$Na_2Ti_3O_7$ spaces respectively, including all known sodiated titania structures (bronze, post spinel, layered, sodium titanate) as well as the common TiO_2 polymorphs of interested here (rutile, brookite, anatase). In the case of Na^+ intercalation, we consider both isolated defects, and symmetrically distinct orderings on the possible interstitial sublattices in each phase and obtain the lowest energy configuration across all Na_xTiO_2 compositions. To access the Na_2O-defect thermodynamics, we enumerate dilute Na_2O in TiO_2 defect configurations, formed by creating a Ti^{4+} vacancy and charge compensating it with 4 Na^+ ions, over all likely configurations of the sodium ions. In all cases, to correct the well-known problem of reproducing the energy of rutile versus brookite and anatase [42], brookite and anatase phases are shifted to +0.007 meV/TiO_2 and +0.023 meV/TiO_2 with respect to pure rutile respectively, based on experimentally-obtained enthalpies of the three phases [19]. While no similar correction enthalpies are known for the bronze, post spinel, and layered phases, no enthalpy shift of these phases within expected DFT error ranges changes which phase is stabilized in both the Na and Na_2O cases.

4. Results and Discussion

As reports of brookite TiO_2 via PLD are sparse, to summarize this chapter, we document the formation and stability of the brookite structure from PLD deposited amorphous films that are subsequently annealed. To establish the presence of brookite in thin films we use 2D synchrotron x-ray diffraction, Raman spectroscopy, and high-resolution transmission electron diffraction. We show, using energy dispersive x-ray spectroscopy that on Na-containing eagle XG glass none of the Na from the substrate migrates into the TiO_2 film. This demonstrates that Na is not needed to stabilize the brookite structure. Furthermore, theoretical calculations of Na intercalation into the TiO_2 matrix using density functional theory show that brookite is never the most stabile polymorph, no matter the amount of Na added. We then conclude our initial observations of brookite thin films with an observation that the amount of brookite in thin films correlates with the thickness of the film, an observation that warrants further investigation.

As our initial findings [44] of brookite in thin films via PLD were accompanied by a few open claims, the next section examines some of these claims in more detail. First, we explore brookite formation relative to the center of the deposition plume and find that particle energetics do not play a major role in brookite formation, further suggesting thickness as a control parameter. We find that high-fraction anatase films are also obtainable in the same range as high-fraction brookite films and we propose that a parameter closely related to the film thickness, the average deposition rate, can explain the anomalies found in the phase fraction vs. thickness. The average deposition rate dependence can be justified when considering the particles supplied to the film during deposition or how the flux of particles at the surface affects oxygen content in the film. We show, by directly varying the oxygen pressure during deposition, that there is a very strong polymorph formation trend, with low deposition oxygen pressures producing rutile, high deposition pressures producing anatase and brookite is produced with pressures in between. Second, to justify claim that the visual identification of brookite in the optical microscope is due to the difference in index of refraction between the polymorphs we use hyperspectral reflectivity mapping. This allows us show that rutile has a higher reflectivity for UV wavelengths of light while brookite is the most reflective for visible wavelengths, further supporting the claim that the optical contrast is manifest from index of refraction

contrast between polymorphs. Then once the open claims from our initial findings are cleared up we dive a little deeper into brookite formation with in-situ optical microscopy/Raman spectroscopy.

Since the brookite structure is identifiable via optical contrast, in-situ annealing of amorphous precursors is used to identify growth rates, nucleation rates, and the activation temperature needed for brookite growth. We find that while previous anneals up to 400°C produce high-fraction brookite (from the appropriate amorphous precursor), 250°C is sufficient to observe brookite as the first polymorph to form, with anatase formation following, suggesting that brookite may be acting as a substrate for anatase during heterogeneous nucleation of the two polymorphs [52]. Furthermore, altering thermal treatment conditions, such as annealing temperature and ramp rate, does not appear to alter the resultant brookite content, additionally pointing to the deposition conditions for the amorphous precursors as the deciding factor in the crystallization process. We begin this chapter with our initial observation of brookite growth and its independence from Na helper ions.

4.1. High-fraction brookite films from amorphous precursors [44]

4.1.1. Theory

Based on a variety of hydrothermal and sol-gel brookite synthesis recipes, a common claim is that the presence of sodium during TiO_2 growth promotes the formation of the brookite phase [5] [6]. To investigate the thermodynamic feasibility of this claim, we evaluate the thermodynamics of sodium incorporation into various known TiO_2 phases. This analysis follows by analogy to the recently reported role of alkali ions in the formation of MnO_2 polymorphs through the stabilization of off-stoichiometric intermediate products [23]. To identify possible off-stoichiometric intermediates, we examine the formation of partially sodiated Na_xTiO_{2+y} compounds, with Na^+ incorporated into the Ti-O matrices of each phase (rutile, brookite, and anatase, as well as the bronze, layered, and postspinel structures which are known to form in the Na-TiO_2 space [53], so that the Na_xTiO_{2+y} phases may template the growth of a particular Ti-O framework. To enumerate the Na_xTiO_{2+y} structures that may play a role in such a mechanism, we consider Na^+ incorporation either through the partial reduction of Ti^{4+} to Ti^{3+}, or the formation of Ti^{4+} vacancies (equivalent to the incorporation of Na_2O). Note, we do not consider the incorporation of purely interstitial Na_2O as none of the TiO_2 polymorphs contain interstitial sites large enough for such defects. We then evaluate the stability of these structures by

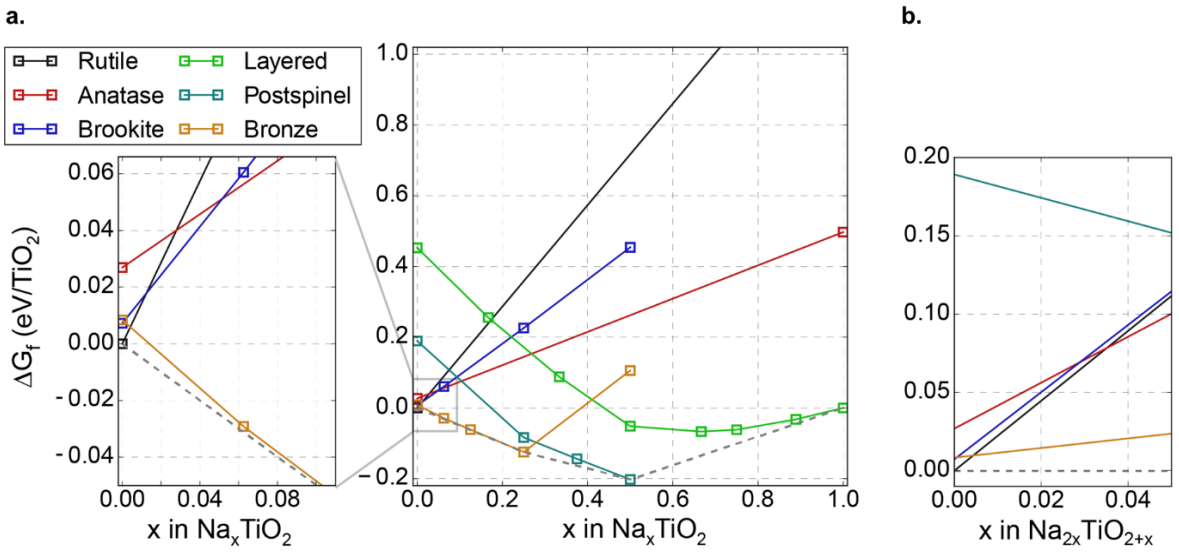

Figure 4.1 Computed low-temperature free energies of (a) Na_xTiO_2 and (b) $Na_{2y}TiO_{2+y}$ compounds, with Ti-O frameworks constrained to those of known TiO_2 phases, as a representative sample of structure selection in the Na_xTiO_{2+y} chemical space. The dotted lines denote the global thermodynamic equilibrium in each composition space.

comparing their energies to that of all known phases in the Na_xTiO_2 and $Na_{2y}TiO_{2+y}$ spaces, regardless of Ti-O framework.

The low-temperature, low-pressure thermodynamics of Na_xTiO_{2+y} compounds, shown as heats of formation in Figure 4.1(a) and Figure 4.1(b), do not support the previously hypothesized role of sodium in brookite formation, at least via the formation of a bulk-sodiated intermediate. In the case of Na^+ intercalation alongside $Ti^{4+/3+}$ reduction, the stabilized phases are TiO_2-bronze at low sodium content, post-spinel at intermediate sodiation, and layered-TiO_2 at high sodiation. These results are consistent with both reported crystal structures in this space [53], and the observation that small levels of sodiation appear to favor the TiO_2-bronze phase [2]. Similarly, Na_2O incorporation is most favorable in the TiO_2-bronze phase, and generally leads to the well-known $Na_2Ti_3O_7$ titanate structure, which is not topotactically related to any of the TiO_2 polymorphs we consider. While these results are obtained for zero-temperature conditions, the large difference in Na-defect energies seen in Figure 4.1 would make the entropic stabilization of sodiated brookite over the competing phases highly unlikely. Of course, it is possible that the role of sodium in previous experiments was not to influence the relative stability of TiO_2-phases through bulk incorporation -- for example, sodium may selectively influence the surface energies of specific TiO_2 polymorphs, thereby affecting their relative nucleation kinetics, analogous to the role of Mg^{2+} ions in influencing $CaCO_3$ polymorphism [54]. Nonetheless, our

analysis suggests that sodium may not be essential to brookite formation, motivating our further experimental study of brookite growth in both sodium-containing and sodium-free media.

4.1.2. Observation of brookite in films on different substrates

Amorphous TiO_2 films deposited on a variety of amorphous substrates, and annealed as described in the methods section, consistently produce crystalline films with varying quantities of brookite and anatase, and sometimes rutile. As we will show these polymorphs form regardless of whether the substrate is sodium-free (pure fused silica (a-SiO_2) or Si with thermally-grown oxide) or sodium-containing glass (Corning Eagle XG (EXG) with low Na content, or soda-lime-silicate (SLS) with high Na content). Na clearly can play no role in the brookite formation on the Na-free substrates. We detail below the identification of various titania phases in a typical film deposited on low-Na EXG glass. Notably, we find no evidence of Na migration into that film. If sodium incorporation were indeed favorable, sodium migration from the substrate would have produced sodiated TiO_2 [2] [3] [4]. We find the fraction of brookite produced in this process is controlled by the thickness of the film and the time and temperature of the anneal, rather than the substrate and the presence of Na^+.

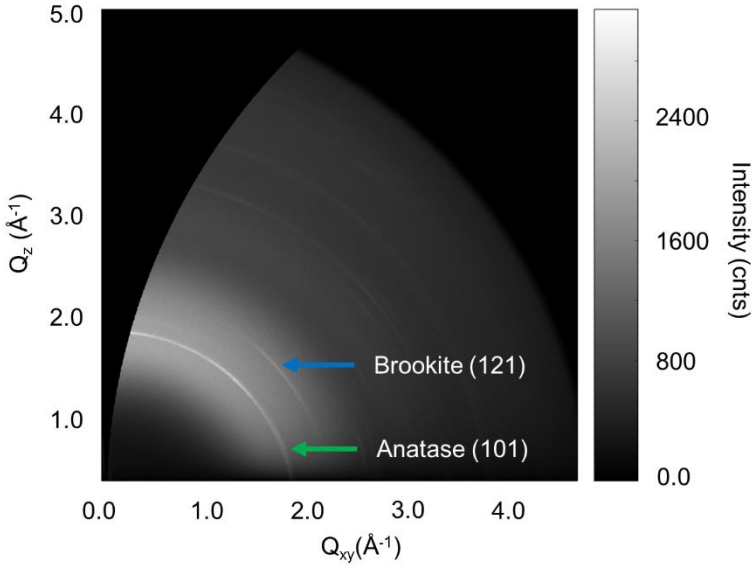

Figure 4.2: 2D XRD pattern of a TiO_2 film after annealing. The strongest peaks are brookite (121) at Q = 2.166 Å^{-1} and anatase (101) at Q = 1.787 Å^{-1}. Brookite (121) has a limited χ range, indicating that brookite crystallites are preferentially oriented.

X-ray diffraction (XRD) is used for phase identification of the different TiO_2 polymorphs as shown in Figure 4.3(a). Such spectra show the XRD signal integrated over the full polar angle χ. Further information about the orientation of the film is evident from examination of the 2D XRD pattern in Fig. S1 where χ is measured along the azimuthal direction. This 2D image shows that brookite is preferentially oriented because the (121) reflection is confined to a small range of χ, while anatase is

much less oriented, with its (101) reflection appearing nearly isotropic. We do not know why the brookite is oriented, but the observation suggests that brookite peaks could be missed in conventional XRD geometries that see only the out-of-plane diffraction at $\chi = 90°$.

Figure 4.3(a) shows background-subtracted, integrated 2D XRD spectra of TiO_2 films, 58 nm and 52 nm thick, on Na-free fused SiO_2 and Na-containing EXG glass substrates respectively, obtained after annealing. The strong brookite signature is evident in films on both Na-containing and Na-free substrates as evident by the XRD peak at Q = 2.17 $Å^{-1}$. This result shows that films of the same thickness that are annealed under the same conditions can produce similar mixed phase brookite and anatase films regardless of the presence of Na in the substrate.

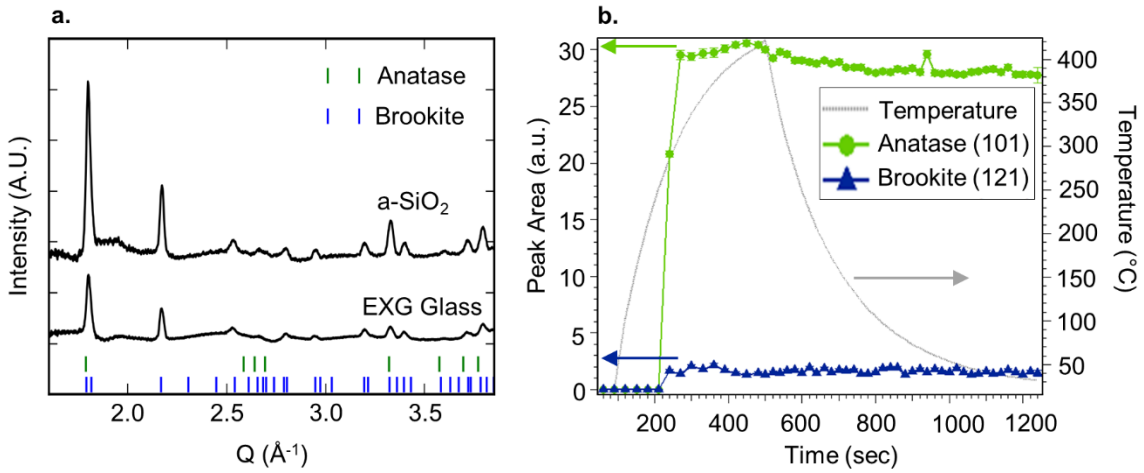

Figure 4.3: (a) XRD patterns of annealed TiO_2 films grown on a-SiO_2 and EXG substrates. The brookite and anatase phases appear in similar proportions in films (58 nm and 52 nm thick respectively) on both substrates. (b) The integrated peak areas for brookite (121) [blue] and anatase (101) [green] on a 65-nm film, grown on EXG, as a function of time and temperature during the anneal indicated by the gray line. Both polymorphs crystallize at ~290°C.

To further explore the annealing process and progression of the crystalline phases, we use in-situ XRD during annealing. Figure 4.3(b) shows the in-situ XRD evidence from a 65-nm TiO_2 (measured by HRTEM) film on amorphous EXG glass annealed in N_2 according to the annealing profile shown in gray. Brookite is tracked by the (121) peak at Q = 2.166 $Å^{-1}$ and anatase by its (101) peak at Q = 1.787 $Å^{-1}$. These peaks provide the clearest signature of the phases of interest because they are strong and relatively isolated, with minimal overlap from peaks from other polymorphs. Here we observe the crystallization of brookite and anatase TiO_2 phases at ~290°C. When the experiment is repeated, we consistently observe that the anatase and brookite polymorphs form concurrently. The polymorphs quickly achieve their final steady-state phase fractions, as evidenced by the lack of

change in peak area after 200 secs. In contrast to crystallization from solution, which is often dominated by one polymorph at a time [55], the concurrent formation of two separate polymorphs here suggest independent nucleation events, likely at different locations of the substrate. There is minimal transformation of the two phases after formation. Gibbs' phase rule suggests that there can only be one polymorph at equilibrium in the film at a time, so the persistence of a two-polymorph thin film suggests slow coarsening kinetics, which is likely due to limited transport kinetics in thin-films.

Figure 4.4 shows optical and Raman images of the mixed-phase brookite/anatase film in Figure 4.3(b). Figure 4.4(a) is an optical image, with clear contrast evident on the micron length scale. The lighter regions, labeled B, are characterized by the Raman spectrum in Figure 4.4(b) which matches the brookite spectrum in the RRUFF database (RRUFFID R050591) [46]. The darker regions, labeled A, yield the Raman spectrum in Figure 4.4(c), which matches anatase (RRUFFID R070582) (52). With the Raman shift tuned to 319 cm^{-1} (brookite) and 144 cm^{-1} (primarily anatase), the laser is scanned over the region marked by the red square in Figure 4.4(a), and the 2D maps in Figure 4.4(d) and Figure 4.4(e), respectively, are obtained. The shapes evident in the optical image, which

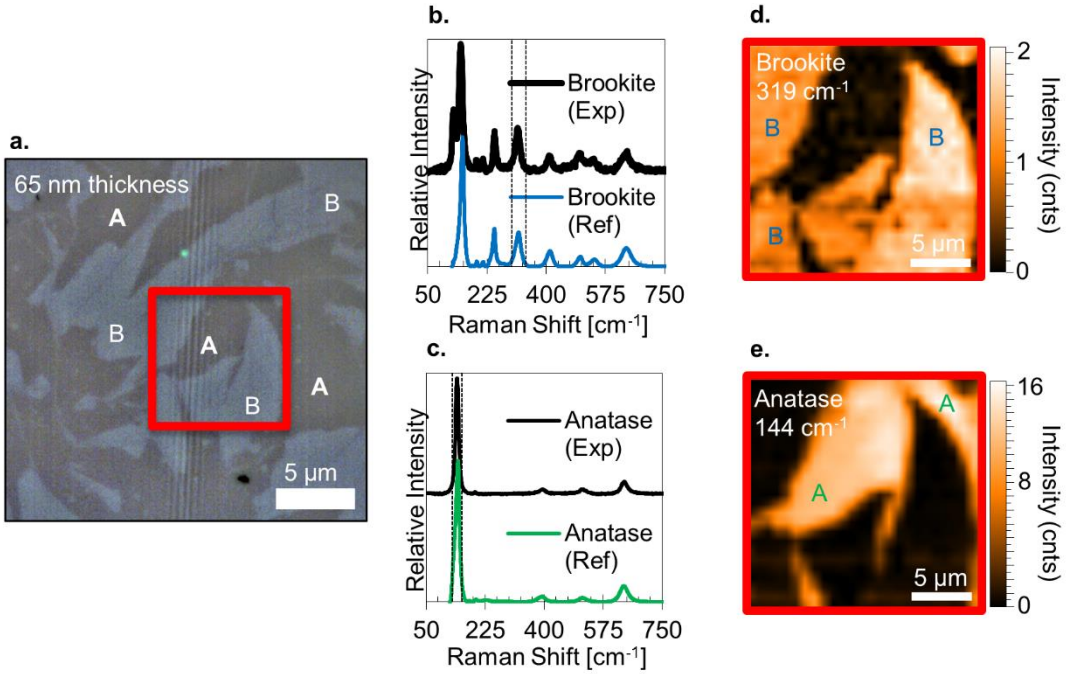

Figure 4.4: (a) Optical image of a 65-nm TiO_2 film on EXG glass. Regions marked B yield the Raman spectrum for brookite in (b), while those marked A yield the anatase spectrum in (c). The 2D Raman maps at 319 cm^{-1} (d) and 144 cm^{-1} (e) show that the color variations in the optical image correlate with a particular polymorph. The brookite: anatase ratio in this film is 50:50 and no rutile is observed. The dotted lines in (b) and (c) indicate the wavenumber range over which the Raman intensity maps in (d) and (e), respectively, are acquired.

presumably result from refractive index contrast (n_{rutile} = 2.72, $n_{brookite}$ = 2.64, $n_{anatase}$ = 2.53) [56], are replicated in the Raman maps, giving an unambiguous polymorph identification. The optical contrast therefore provides a quick and convenient "first-cut" polymorph identification method, which can then be confirmed with Raman or electron microscopy. From the 2D Raman maps, it is easy to convert the A and B areas to polymorph fractions, which for this film is 50% brookite to 50% anatase. Associating the area with a volume phase fraction assumes the surface structures permeate the film.

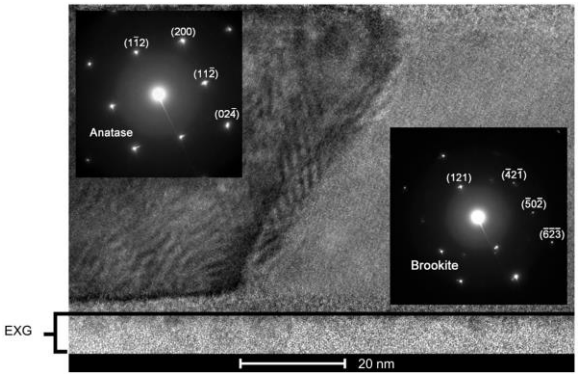

Figure 4.5: HRTEM image of a 50-nm TiO_2 film on EXG glass. The selected area electron diffraction patterns in the insets indicate that the grain on the left is anatase and on the right is brookite. The S-shaped grain boundary is approximately 20 nm wide.

Cross-sectional TEM analysis in Figure 4.5 shows that the grains do indeed occupy the entire film thickness and can be considered columnar on a micron-scale. Figure 4.5 also provides further phase confirmation by the electron diffraction shown in the insets. The TEM image shows an anatase-brookite grain boundary, which changes curvature from the top of the film to the bottom. This S-shape extends over a 20-nm range perpendicular to the boundary. Due to a balance of forces indicated by the point of inflection, boundary mobility and further grain growth are significantly reduced, again suggesting that phase stability is kinetically limited [57]. The in-situ XRD studies in Figure 4.3(b) also suggest a rapid settling into a morphological configuration after a rapid nucleation, shown by the plateau in intensity after crystallization. Further experiments are needed to understand the details of the nucleation and growth of the polymorphs and the nature of the phase boundary.

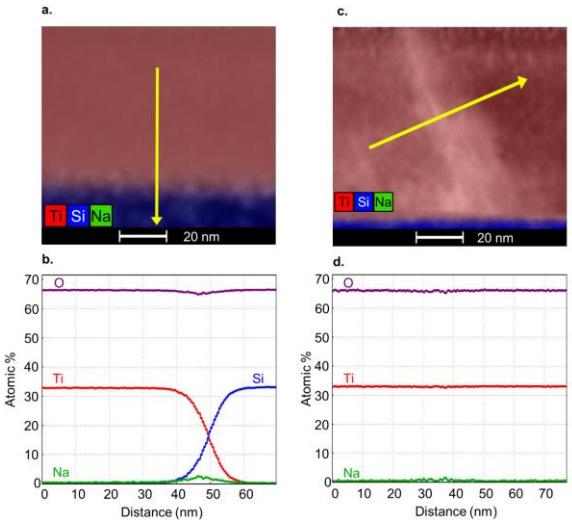

Figure 4.6: Elemental EDS maps (a, c) of composition of the TiO_2 film in Fig. 5, and the atomic concentration (b, d) along the indicated line. Plots (a, b) trace the substrate/film interface and plots (c, d) highlight the grain boundary. Na (green) is below the detection limit in the TiO_2 film and accumulates near the film-substrate interface.

EDS analysis of Ti, O and Na is shown in Figure 4.6 of a film grown on EXG and annealed in a manner like the film in Figure 4.3(b). The TiO_2 stoichiometry is confirmed by EDS and there is no change in stoichiometry at or near the grain boundary (<0.35 at%). There is no evidence of Na migration into the film, nor into the grain boundary. There is a clear accumulation of Na in the substrate near the substrate film/interface, however.

4.1.3. Film thickness and polymorph fraction

We have reproduced the results described above in many films made on different amorphous substrates that are Na-containing (EXG and SLS) and Na-free (a-SiO_2 and Si with 100 nm of thermal oxide). Figure 4.7 shows the results of a phase fraction analysis of many samples annealed with the standard protocol described in the methods section with hold times of 0 or 1 min at 400°C. There is a thickness gradient across most films, which allows the observed phase fraction to be correlated to the thickness of the film in that region. The data in Figure 4.7. represent 10 different depositions, with the different classes of substrate denoted by the symbol shape. Each deposition yields several entries on the plot because the film thickness varies across the sample. At each thickness, there are four color-coded points representing the brookite, anatase, rutile and amorphous fractions, averaged over an area approximately 150 µm x 150 µm. One striking feature is that films with brookite as the major phase (above 70% and up to 95%) are clustered in the thickness range of 45 to 65 nm. At the lowest thicknesses, below ~30 nm, anatase is the major phase. Between 30 nm and 45 nm, brookite as the dominant crystalline phase is accompanied by the presence of an amorphous component. This transition corresponds with the size-dependent stabilization order identified by Ranade *et al.* [19] for TiO_2 crystallites in solution. Rutile is absent or a minor phase for most of our films; examples of rutile-containing films are given in Figure 4.23, Figure 4.25, Figure 4.26.

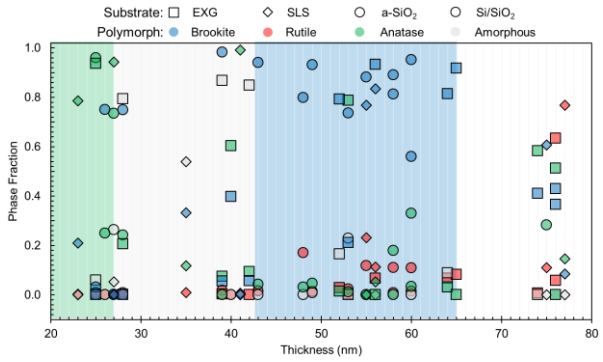

Figure 4.7: Phase fraction of brookite (blue), rutile (red) and anatase (green) polymorph or amorphous component (gray) in TiO_2 films as a function of thickness. Na-free a-SiO_2 and Si/SiO_2 (circles), low-Na EXG (squares) and high-Na SLS (diamonds) substrates are represented. The uncertainty in thickness is ±5 nm for d < 50 nm and ±3 nm for d > 50 nm.

4.2. TiO_2 Polymorph Selection

Polymorph selection is a complicated process in TiO_2, and brookite is difficult to synthesize. This section documents some of these complications and shows that film thickness may not be the only factor controlling brookite synthesis. Other related factors are investigated, including the deposition rate and the position in the plume where the "ideal thickness" occurs. This section ends with an x-ray diffraction evaluation of thin films created from precursors deposited using a series of different oxygen pressures showing that oxygen pressure (as a proxy for oxygen content) is an important factor in polymorph selection in TiO_2. We begin this investigation by first considering the large surface area depositions which show a distinct thickness gradient related to the shape of the plume and the particle energetics within the plume.

4.2.1. Plume Position and Deposition Rate

Plume Position: To determine whether particle energetics within the laser plume affects polymorph selection, we use two different depositions with two different thickness gradients. Figure 4.8 shows two tests using large surface area depositions where thickness gradients observed across

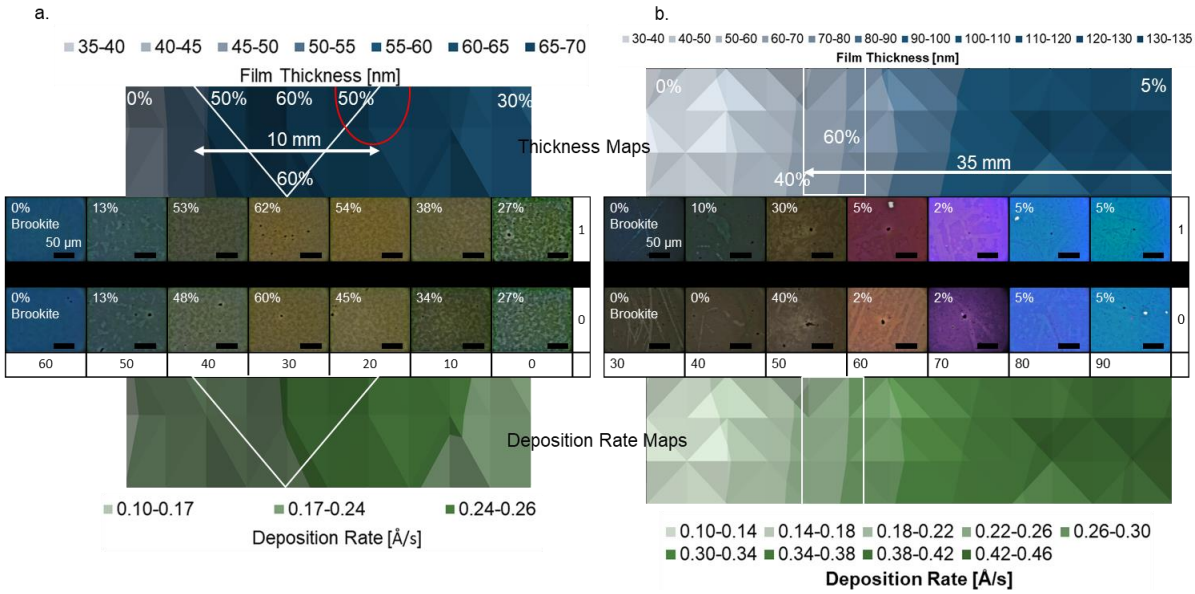

Figure 4.8: (a) and (b) consist of 3 profiles each of two depositions. (a) is a 1 mTorr pO_2 deposition with max thickness of 70 nm. The thickness profile on top (blue) with brookite percentages labeled and high fraction brookite range within the triangular region. Below the thickness map is a morphology map consisting of x50 microscope images in approximately 5 mm intervals across the sample. The numbers in the bottom row and left most column are cell identifiers used to calibrate positions across multiple systems. The bottom image is the corresponding deposition rate profile with the high fraction brookite region located inside the triangle section. (b) is the same set of images as (a) but for another 1 mTorr pO_2 deposition with max thickness 135 nm. The white rectangle indicates the high brookite fraction section.

each sample allow testing of multiple thicknesses and the qualitative comparison of the average kinetic energy of the particles bombarding the surface during deposition. The center of the plume is located where the largest amount of mass is transferred from the target to the substrate, assuming no resputtering (back splashing) from the substrate surface. Hence, the thickest section of the film in Figure 4.8(a) (red circle) identifies the center of the plume (the plume center is off the thickness map to the right for Figure 4.8(b)). As is shown by Vaziri et al. [58], the average kinetic energy of the ions transmitted during deposition drops off drastically the further from the center of the plume the material is deposited. The thickness maps (blue contours) for Figure 4.8(a) and Figure 4.8(b) represent the two situations where the ideal brookite thickness (60-70 nm, Figure 4.7) appears near the center of the deposition (Figure 4.8(a), $d_{max} = 70\ nm$) and the other, far from the center of the deposition (Figure 4.8(b) , $d_{max} = 130\ nm$). As the morphology maps show, for both depositions the highest fraction of brookite is found in the 60-70 nm thickness range. Since these two depositions show brookite forming under very different particle energetic conditions (one near the center of the plume and the other far from the center of the plume), one might conclude that film thickness is the stabilizing mechanism for brookite. However, deposition rate correlates equally as well as film thickness and can additionally explain some of the high fraction anatase films found in the ideal brookite thickness range. As the inset in Figure 4.9 shows, films within the same thickness window (60-70nm) can also form high-fractions of anatase instead of brookite.

Deposition Rate: Another deposition control parameter that also affects polymorph formation is the average deposition rate. The average deposition rate, $\langle v_D \rangle$, is given by $\langle v_D \rangle = \left({}^{d}/_{n_L}\right) f_L$, where d is the film thickness in angstroms, n_L is the total number of pulses used for the deposition, and f_L is the laser repetition frequency in hertz. The only parameter which is measured in $\langle v_D \rangle$ is the film thickness (determined from thin film interference using transmission and reflection spectroscopy), the others are fixed by the deposition system. The average deposition rate is interpreted as the rate at which material accumulates on the surface of the substrate. Below the morphology maps in Figure 4.8 are the corresponding deposition rate maps (green contours) with the high-fraction brookite regions identified. In Figure 4.8 the high-fraction brookite regions correspond to the same deposition

rates ($0.18\text{Å}/s < \langle v_D \rangle < 0.26\ \text{Å}/s$) suggesting an equivalent correlation to that of film thickness. The advantage deposition rate is a better control parameter than film thickness alone because now we can discuss the environment of the amorphous film as it is formed during deposition and correlate it with other control parameters such as deposition oxygen pressure. However, before we can discuss the deposition environment of the amorphous film we must ensure the repeatability of the correlation between phase fraction and average deposition rate.

First, consider the inset in Figure 4.9 as compared with the main plot. When thickness is considered alone as the parameter controlling the phase content in the thin films, a large grouping of mixed phase films can be obtained for thicknesses less than 100 nm. In the "ideal" brookite thickness range one can see that it is also possible to obtain high-fraction (>0.6) anatase films, as well as some high-fraction (>0.8) rutile films. This suggests that there must be some other parameter affecting the resulting crystalline products in this thickness range. So, if we now look at the main plot in Figure 4.9, we can see that the large cluster of mixed results shows two distinct trends. The high-fraction brookite containing films all appear within the "ideal" brookite thickness range but with higher deposition rates ($0.25\ \text{Å}/s < \langle v_D \rangle < 0.7\ \text{Å}/s$), while all the high-fraction anatase films appear for almost all thicknesses tested but typically form from films made with lower deposition rates ($\langle v_D \rangle < 0.2\ \text{Å}/s$). There are one or two films tested which showed higher amounts of rutile at the higher deposition rates, but without additional films in this range the highest deposition rates only suggest that rutile may be favored. Figure 4.9 does not show what forms in the >60 nm thickness range and >0.25 Å/s deposition rate range because once the ideal brookite thickness range

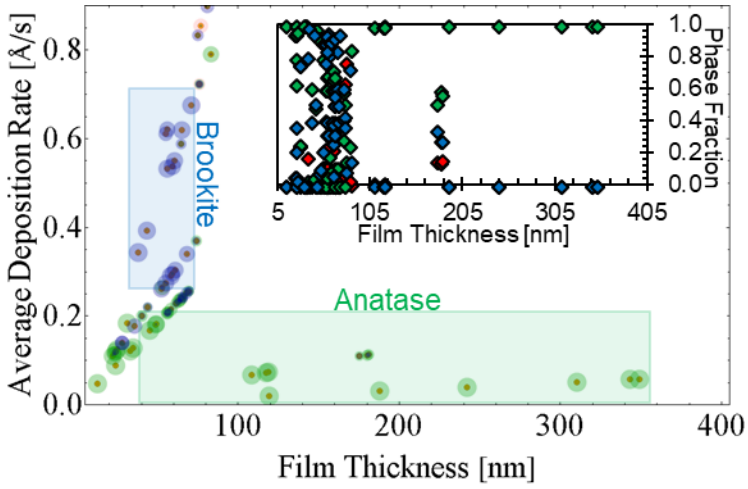

Figure 4.9: Average deposition rate and film thickness as functions of Raman phase fraction. Colors correspond to blue for brookite, red for rutile, and green for anatase. Size of the bubbles corresponds to the polymorph fraction. Inset is phase fraction as a function of film thickness alone for the same data.

is passed (while still within the ideal deposition rate range) the films switch to a mixed morphology, dominated by anatase that is difficult to separate definitively from the brookite (an example of this is shown in the morphology map of Figure 4.8(b)). This suggests that there may be some kinetic or growth parameter during annealing which additionally affects the final crystalline product. The only explanation for the thickness dependence that we can offer is the possibility of the thickness confining the particle sizes in one dimension to facilitate polymorph selection, while the deposition rate provides the off-stoichiometry needed to form brookite.

On an unheated substrate, the species only have the energy they hit the surface with, and any residual energy (in the form of heat transferred locally by particles deposited on the substrate) from the previously deposited species, to form bonds and clusters as the film grows. This means not only that a lower deposition rate will facilitate less off-stoichiometry, while a larger deposition rate will favor more off-stoichiometry. One way to see that this is the case is by considering the distance L_0 at which half the atoms stop moving away from the target, as proposed by Strikovski and Miller [59]. L_0 for a specific PLD system is defined by

$$L_0 = f\left(\frac{3\mu N_0}{n_g}\right)^{1/3} \qquad 4\text{-}1$$

$$f^3 = \frac{1}{2}\left[(3\mu - 1) + \sqrt{(3\mu - 1)^2 + 12}\right] \qquad 4\text{-}2$$

where $\mu = M/m$ the ratio of atomic masses of the ejected species and the background gas species, $n_g = P_g/kT = 3.3\ x\ 10^{13}$cm^{-3} is the gas density at room temperature and pressure $P_g = 1$ mTorr, and N_0 is directly related to the average deposition rate $\langle v_d \rangle / f_L$ in thickness per pulse for a film deposited at some target-to-substrate distance d,

$$N_0 = \frac{\langle v_d \rangle}{f_L} n_L d^2 \qquad 4\text{-}3$$

and a concentration of deposited atoms n_L (~$5\ x\ 10^{22}$ cm^{-3} for most solids). Now as for the deposition of TiO_2 ($M = 79.9$) in a background of 1 mTorr oxygen ($m = 32, \mu = 2.5, f = 1.2$) at a target-to-substrate distance of $d = 11.5\ cm$ we find that for low deposition rates ($\langle v_D \rangle < 0.2$ Å$/s$) half the particles in the plume are turned back at a distance $6 < L_0 < 8$ cm. Since most of the particles in

the plume are scattered before reaching the substrate for low deposition rates, the ones that do reach the substrate will be less dense and more disperse, and without additional substrate heating may lack sufficient energy to move any significant distance to merge with other particles deposited on the surface at the same time. This means that more surface area is exposed to the oxygen atmosphere between each pulse, resulting in a film with higher oxygen content. Then for higher deposition rates ($\langle v_D \rangle > 0.7$ Å$/s$), we find $L_0 \sim 12$ cm suggesting that most of the particles in the plume reach the substrate before being diverted by the background gas, and with the higher density of particles deposited on the surface less mobility is needed before a particle encounters another. This means that less surface area is exposed to the oxygen atmosphere between each pulse, resulting in a film with lower oxygen content. However, we can see from Figure 4.8(b) that there must be some other parameter which limits brookite growth for thicker films, we must conclude that deposition rate and film thickness are not the only important parameters that must be balanced to form brookite.

4.2.2. Deposition Oxygen Pressure (pO_2)

Oxygen Content: The deposition rate combined with the oxygen pressure during deposition may provide the explanation for why thicker films do not form as much brookite. The literature on PLD of YBCO thin films for instance has shown that "the oxidation during growth can be kinetically limited by the availability of sufficient oxygen to oxidize the high flux of cation species" [60], suggesting that a strict control over oxygen pressure during deposition can profoundly affect the resultant crystal structure. Furthermore, in the V-O system it has been shown that the oxygen pressure can be used to directly control the oxidation state of the cations [61]. Thus, we can change the oxidation state of the titanium by two methods, either increase (or decrease) the cation flux during deposition without changing background oxygen pressure or change the oxygen pressure during deposition.

Another important parameter for polymorph selection in the Ti-O system is the oxygen pressure during deposition. There are multiple reports in the literature on the dependence of crystal structure in TiO_2 on the oxygen pressure during deposition. [62] [63] [64] These reports show that at low oxygen pressure rutile is favored and at high deposition pressure anatase. There are very few reports of the dependence of brookite on the deposition oxygen pressure, mostly due to the limited

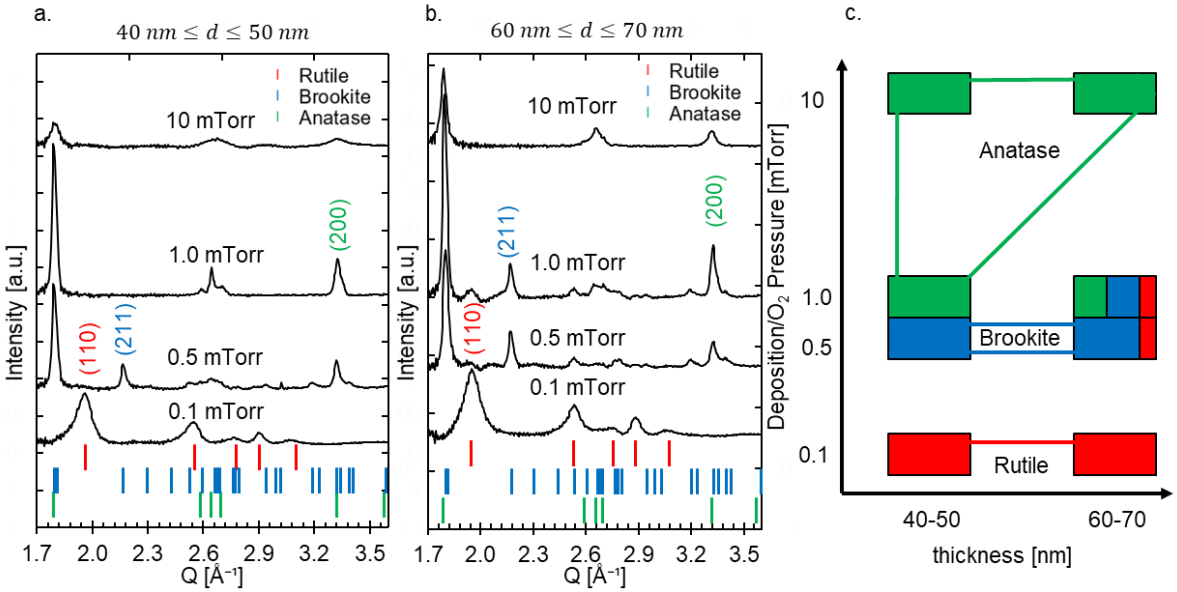

Figure 4.10: χ-Integrated 2D synchrotron XRD data acquired with x-ray wavelength $\lambda = 0.9744\ nm$. (a) and (b) XRD spectra of 2 sets of different thickness, 40-50 nm and 60-70 nm respectively, films all deposited with the indicated oxygen pressure. Reference peak locations are indicated by the vertical lines at the bottom of the plot and important polymorph peaks are identified, red rutile (110), blue brookite (210), and green anatase (200). (c) is a cartoon graph of the different polymorphs identified by the XRD as a function of both thickness and deposition oxygen pressure.

number of reports of vapor deposited brookite. Figure 4.10 is a series of x-ray diffraction data collected at the Stanford Synchrotron Radiation Light source with films of different thicknesses (40-50 nm and 60-70 nm), deposition rates, and deposition oxygen pressures (0.1 mTorr, 0.5 mTorr, 1.0 mTorr, and 10 mTorr). Figure 4.10(a) is the full XRD spectra for the 2D-χ-integrated data with background subtraction. Each XRD spectrum is compared with all three reference spectra (00-021-1272 for anatase, 01-084-1284 for rutile, and 01-076-1937 for brookite) from the International Center for Diffraction Data (ICDD) for polymorph phase identification. In Figure 4.10(a)-(b), the rutile (110) (1.96 $Å^{-1}$), brookite (211) (2.17 $Å^{-1}$), and anatase (200) (3.32 $Å^{-1}$) peaks are singled out to emphasize the presence of each polymorph. For all thickness ranges, when the deposition pressure is low, rutile is favored, and for high pressures anatase is favored. For pressures in between, there is a window of opportunity for brookite to form.

This strong dependence on oxygen content can be used to justify the deposition rate as the control parameter for crystalline formation in TiO_2, and the ordering of the polymorphs with respect to deposition pressure. First, consider that for many materials an oxidation layer is formed once exposed to atmosphere. Silicon for instance forms a native oxide layer of up to 20 Å thickness of a-SiO_2 [65] when exposed to atmosphere. Titanium on the other hand forms an interesting hierarchical structure, when exposed to small amounts pure oxygen in vacuum, where the exposed surface of the oxide layer is fully oxidized TiO_2 while the interface between the native oxide and the titanium substrate tends to favor suboxide formation [66]. The fully oxidized layer, according to Lu et al. [66] accounts for about 20% of the total oxide layer thickness. Thus, if during deposition each pulse does contain a high enough flux of cations it is likely to fully oxidize before becoming thick enough to form a complete film. This suggests that a delicate balance of the oxygen content in the film by strict control of the deposition rate and the oxygen atmosphere is needed to facilitate the formation of brookite.

Amorphous to Crystalline Band Gap Energy: Since the crystalline product shows such a strong dependence on oxygen deposition pressure we can use this to examine the optical properties of the amorphous precursors and how they relate to the final crystalline product as a function of the oxygen content in the film. To examine the band gap dependence on film thickness for both the

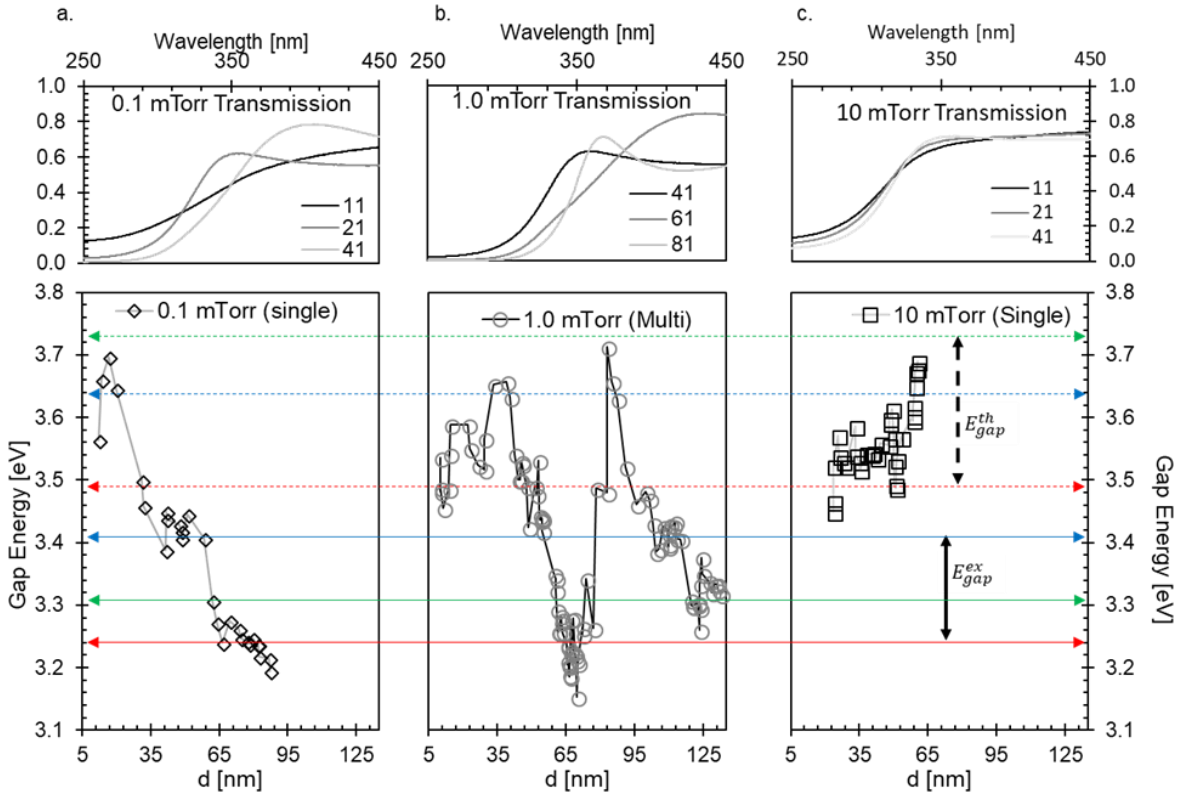

Figure 4.11: Transmission vs light wavelength across 3 amorphous samples at deposition oxygen pressures 0.1 mTorr (a), 1.0 mTorr (b), and 10 mTorr (c) with the corresponding band gap values as function of thickness. The colored lines (blue for brookite, red for rutile, and green for anatase) in the band gap as a function of thickness plots indicate the theoretically predicted band gap values (dashed) and experimentally determined band gap values (solid) for reference. The plot label in the transmission vs wavelength plots corresponds to the large area deposition cell values described in Figure 3.1.

amorphous precursors and the post-anneal crystalline product, specular transmission measurements are used to map the large surface area films. The transmission spectra are then fit for band gap energy and film thickness using the SCOUT optical data processing software package. The results for the band gap as a function of film thickness for the amorphous precursors deposited at three different oxygen pressures (0.1 mTorr, 1.0 mTorr, and 10 mTorr) are shown in Figure 4.11(a)-(c) along with representative transmission spectra for each deposition pressure.

As can be seen from the plots in Figure 4.11(a)-(c), the band gap trend as a function of film thickness is very different for each of these deposition pressures for the amorphous precursors. The 0.1 mTorr deposition pressure shows a decrease in the band gap as a function of thickness from 5-65 nm. The 1.0 mTorr deposition pressure sample also shows a decrease in band gap below 65 nm thickness but its onset is not until about 35 nm and additionally shows a sharp increase in band gap

around 80 nm thicknesses. Then there is the slight increase in band gap as a function of thickness for the 10 mTorr deposition pressure. Since these samples are all amorphous we cannot say that these band gap energies are associated with an well defined optical transition within a crystal structure, but as we will see Figure 4.12 suggests these trends are indicative of the final crystalline products, post anneal.

Figure 4.12 shows the band gaps as functions of thickness for the annealed samples for the different deposition pressures all separated by the dominant polymorph (> 0.6 fraction) as identified by Raman spectroscopy. The band gap values for each of the polymorphs within the range 50-65 nm are all within the ranges reported elsewhere, 3.26-3.51 eV for rutile [67] [68] [69], 3.3-3.8 eV for brookite [28] [41, 70, 69], and 3.03-3.61 eV for anatase [69] [71] [72] [73]. Though the band gap

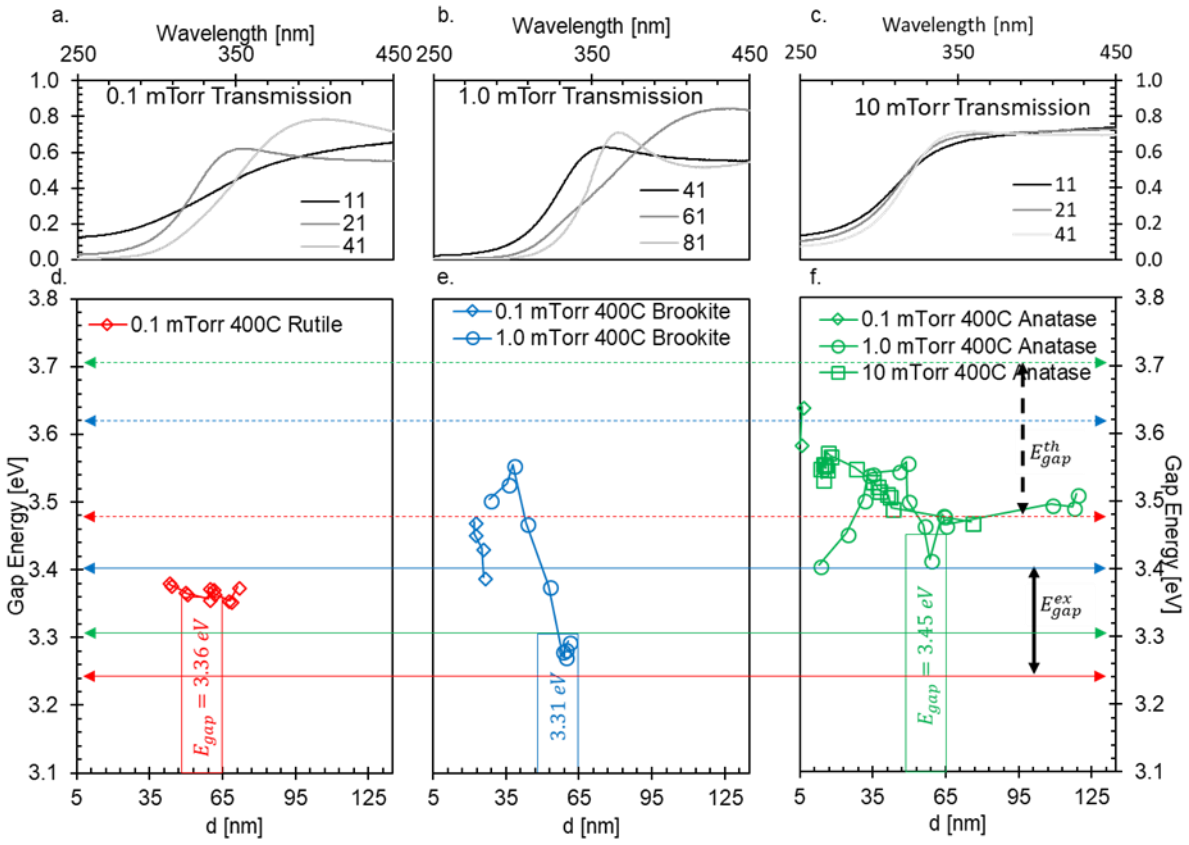

Figure 4.12: Transmission vs light wavelength across 3 deposition oxygen pressures 0.1 mTorr (a), 1.0 mTorr (b), and 10 mTorr (c) all annealed using the 400°C hold RTA profile. (d)-(f) are the different polymorph band gaps as functions of thickness for films with polymorph fractions greater than 0.6. The sample deposition pressure is indicated by the shapes, diamonds for 0.1 mTorr, circles for 1.0 mTorr, and squares for 10 mTorr. The colored lines (blue for brookite, red for rutile, and green for anatase) in the band gap as a function of thickness plots indicate the theoretically predicted band gap values (dashed) and experimentally determined band gap values (solid) for reference.

ranges for each of the polymorphs overlap with each other, complications can arise with the band gap when the crystal structures mix. Castrejón-Sánchez et al. reported in 2014 [74] that when 15% anatase is mixed with rutile the band gap can drop from 3.15 eV down to 2.95 eV, suggesting that small inclusions of secondary phases can drastically change the band gap, suggesting that the trends we see in Figure 4.12 may be due more to polymorph mixing than film thickness.

Each polymorph shows a unique trend as a function of film thickness. Where anatase (3.45 eV) and rutile (3.36 eV) show a realtive stability in the band gap value, brookite shows a strong drop in band gap as the film thickness increases (from 3.55 eV to 3.31 eV for 35-65 nm thickness variation). As the phase fraction as a function of thickness indicates a transition from brookite to anatase as film thickness decreases from 65 nm to 35 nm, this increase in band gap is likely due to an increased influence from anatase. One might be tempted to conclude that quantum size effects are responsible for the band gap increase [75] as brookite becomes thinner, but, at least in the case of anatase, others [75] have reported size quantization effects are not likely for particles of size greater than 1 nm in radius.

Strain and Particle Size: So let us now examine the XRD more carefully to determine the particle sizes and average strain. Another observation in the XRD data is the width of the peaks and how they change with deposition rate and deposition pressure. The broadening of peaks in XRD is directly related to the average particle size and the strain in a material [48]. Each spectrum in Figure 4.10 was analyzed for peak widths for all peaks associated with each polymorph and a Williamson-Hall plot similar to the one in Figure 3.3(b) is used to determine the average particle size and average lattice strain on each polymorph. Figure 4.13(a) shows that the strain is inversely proportional to particle size for each polymorph. Films containing rutile all have high strain and small particle sizes, anatase containing films show a broad range of particle sizes and strain levels from highly strained

small particles to low strain large particles. Brookite on the other hand exhibits two distinct trends, a lower strain trend and a higher strain trend. The higher strain trend contains films that were deposited at 1 mTorr oxygen pressure and annealed up to 400°C using the RTP protocol. Of the lower strain films, one was deposited at lower pressure (0.5 mTorr, and annealed up to 400°C) and the others were annealed at higher temperatures, post initial 400°C anneal, and are the films shown in Figure 4.25($\varepsilon = 0.07\%$) and Figure 4.26($\varepsilon = 0.04\%$). Since the two higher temperature annealed films were treated differently than the rest they are not included in any further analysis, but they do suggest that additional anneals may be one of the pathways to reducing the strain on the brookite structure.

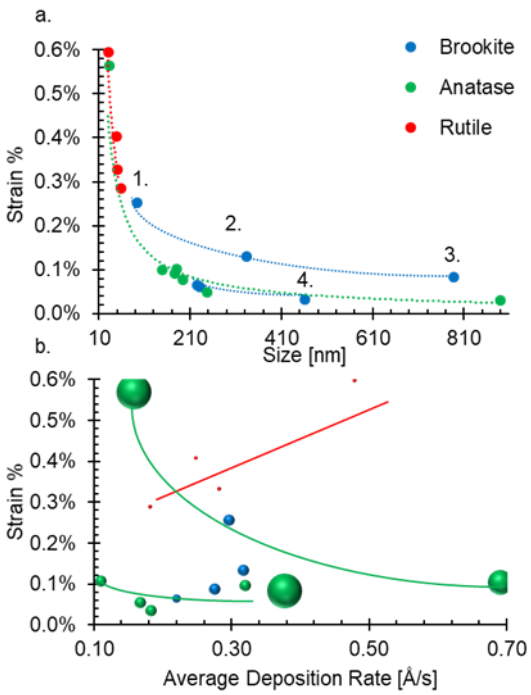

Figure 4.13: (a) lattice strain vs average particle size as determined from Williamson-Hall plots for films with the highest fractions of each polymorph. (b) lattice strain vs deposition rate and deposition pressure for the same films in (a) where the bubble size indicates the deposition pressure (smallest bubble is 0.1 mTorr, and the largest is 10 mTorr).

To illustrate the manifestation of the strain on the brookite film morphology, the dots numbered 1-4 in Figure 4.13 (a) are displayed in Figure 4.14(also labeled 1-4). This series consists of x100 magnification optical images showing the morphological changes in brookite as the strain decreases from left to right. As the strain decreases, the number of identifiable veins also decreases, suggesting that the veins correlate with strain on the brookite structure. In terms of the strain as a function of the deposition rate there does not appear to be a trend for brookite containing films in Figure 4.13(b) and so more data is needed to determine if there is a relationship for brookite with

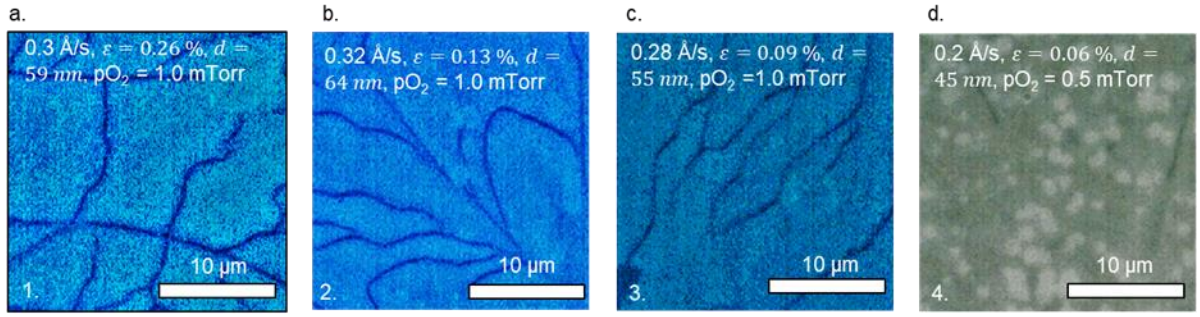

Figure 4.14: Series of x100 optical microscope images showing the morphology as strain decreases. (a) ($\varepsilon = 0.26\%$). (b) ($\varepsilon = 0.13\%$). (c) ($\varepsilon = 0.09\%$). (d) ($\varepsilon = 0.06\%$). As the strain in the film decreases the number of veins decreases as well suggesting that the veins correlate with the strain.

respect to strain, rutile and anatase however do show some interesting features with respect to deposition rate.

Figure 4.13(b) is a bubble plot of the average lattice strain versus the average deposition rate where the size of each bubble represents the relative deposition pressure (large bubbles are 10 mTorr and small bubble are 0.1 mTorr). The lines in this plot are used to indicate the trend and are not best fit lines. The anatase lattice strain shows two different trends with deposition rate, one for higher pressures and one for lower pressures. The higher deposition pressures show a strong inverse proportional relationship, while the lower pressures show a subtle inverse proportional relationship. These two trends could merely indicate a shift from one strain contour to another by using pO_2 as a control parameter, suggesting that lower pressures produce less strained anatase. Rutile, on the other hand, shows an almost linear increase in strain with deposition rate with only a single deposition pressure producing high fraction rutile films.

4.2.3. TiO_2 Thin Film Optical Response: From Spectral to Hyper-Spectral

In this section some of the optical properties of both amorphous and crystalline TiO_2 thin films are shown. The earlier report of the different indices of refraction (n_{rutile} = 2.72, $n_{brookite}$ = 2.64, $n_{anatase}$ = 2.53) [56] as justification for the contrast differences between the three polymorphs is explored in more detail using hyper-spectral mapping, spatially resolved reflectivity.

Hyperspectral imaging: Figure 4.4 shows that the different TiO_2 polymorphs are identifiable via contrast in an optical microscope using a broadband light source. To explore this property in more detail, hyperspectral mapping is used. Figure 4.15(a) is a x50 magnification optical microscope image from the Raman system where each of the regions is identified as either B for brookite, A for anatase, R for rutile, or amorphous. Figure 4.15(b)-(d) are spatially resolved reflectivites (same section of film in Figure 4.15(a)) at $\lambda = 385\ nm$, $\lambda = 406\ nm$, and $\lambda = 435\ nm$ respectively. This series of images shows that from UV to visible light the most reflective sections switch from rutile to brookite, with anatase and amorphous in between. To emphasize this point, the perimeter of each polymorph region is selected and the average reflectivity is calculated for each wavelength using imageJ. Since there are multiple regions for each polymorph an average of the reflectivities is calculated to obtain the reflectivity as a function of wavelength for each polymorph, Figure 4.15(e). Also included in Figure 4.15(e) is the relfectivity of the entire image

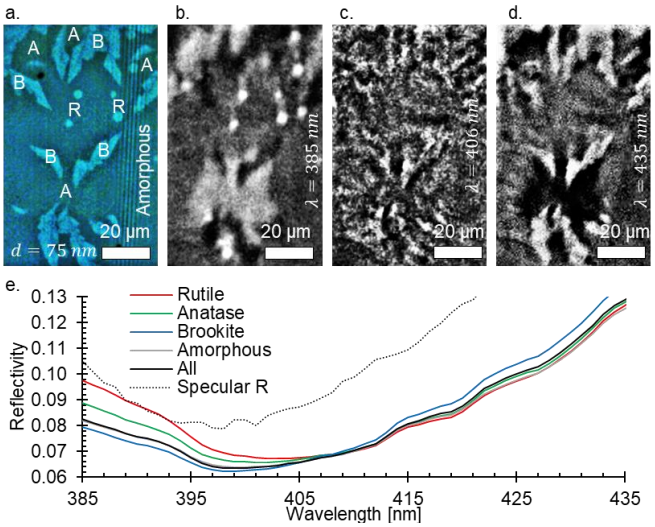

Figure 4.15(a) x50 magnification optical microscope image of a film on Eagle XG glass containing all three polymorph phases labeled R for rutile, A for anatase, and B for brookite. (b), (c), and (d) x40 magnification hyperspectral reflectivity of the same section of film in (a) at light wavelengths, 375 nm, 555 nm, and 765 nm respectively. (e) reflectivity as a function of wavelength for the individual regions identified as rutile, anatase, brookite or amorphous. Also included is a traditional spectral reflectivity spectrum from the same sample close to the same region (as seen by the interference fringe at 400 nm.

and a traditional specrular reflectivity measurement from a region close to the one shown in Figure 4.15(a).

The hyperspectral polymorph reflectivites show that in the UV rutile is the most reflective while in the visible brookite is the most reflective. This change in reflectivity can be attributed to three possible properties of the film, the thickness, the index of refraction, the band gap, or any combination of the three. So let us explore the different possibilities to deterime which one is most likely.

First, if the thickness was the dominant driver of the switch then the fringes in each of the reflectivites should be shifted from each other. Since the fringes at about 400 nm all appear to

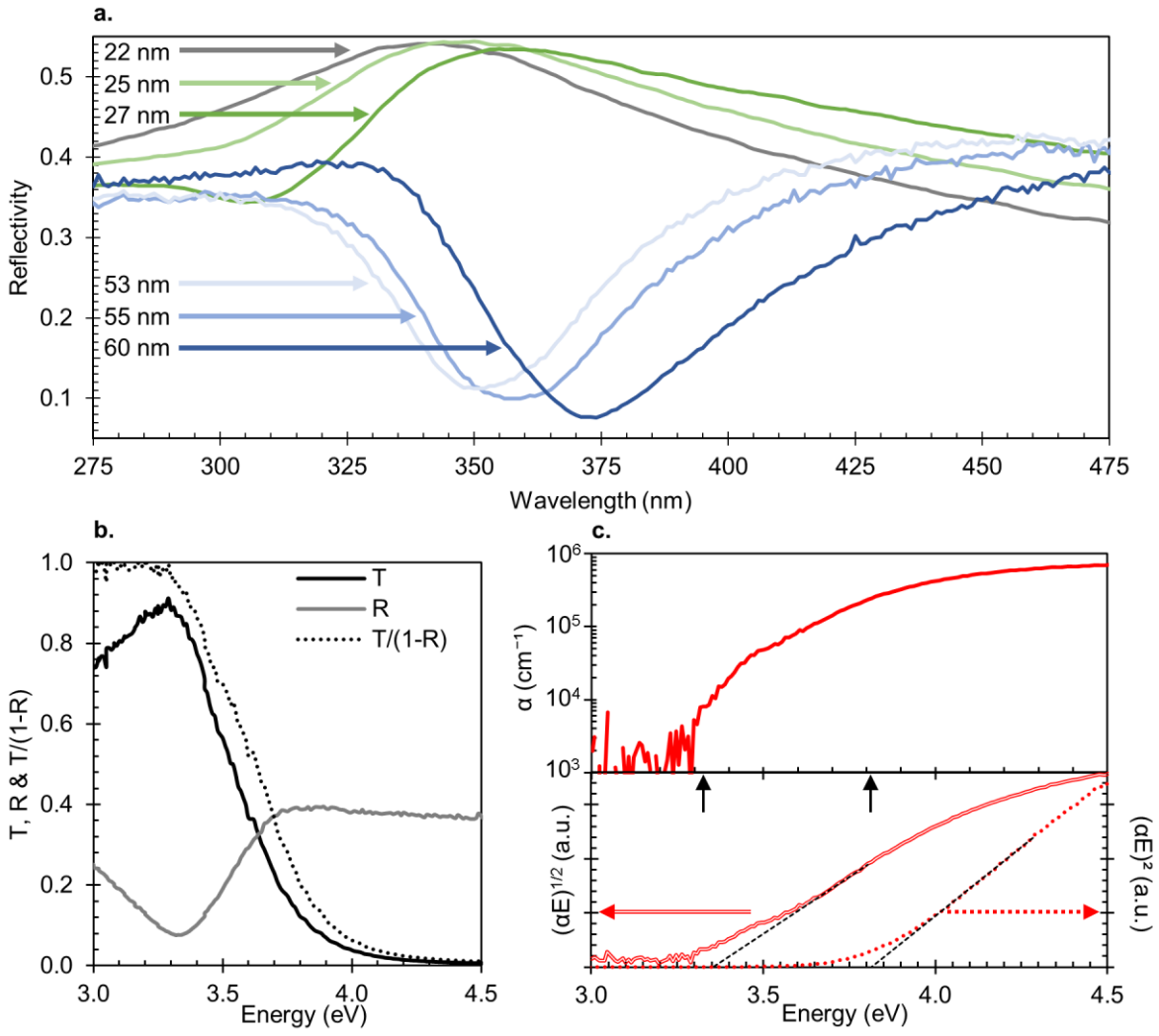

Figure 4.16: (a) Reflectivity as a function of wavelength showing the shift in interference fringes used to determine film thickness. (b) Transmission, reflection and reflection-corrected transmission of a 60-nm high-brookite-fraction film. (c) Absorption coefficient of the film in (b) with arrows labelling the band gaps obtained if the data are analyzed (insets) as indirect (lower value) or direct gap (higher value).

overlap, and upon examination of the NIR region (not shown) the fringes also overlap. To emphasize that the change in relfectivity is not due to film thickness, Figure 4.16(a) shows reflection spectra from different parts of two TiO_2 films along a thickness gradient. The thinner sample (green) contains a single constructive interference fringe that shifts significantly with a 5-nm change in thickness. For the thicker sample (blue), the first constructive fringe is beyond the range shown and a second, destructive, interference fringe has appeared. Thus, the transition in reflectivity cannot be due to a thickness difference between the regions.

Since 385 nm (3.22 eV) is close to where the band gap for rutile should be (3.24 eV) it is likely the increased reflectivity of rutile in the UV is due to light emission from electrons relaxing after excitation across the band gap. The brookite and anatase band gaps are higher in energy, 3.41 eV (364 nm) and 3.31 eV (375 nm) respectively and do not show as strong of an effect in the UV. Figure 4.16(b) shows the transmission and reflection spectra of a 60-nm high-fraction brookite film on a-SiO_2, along with the reflection-corrected transmission spectrum $T/(1-R) \approx e^{-ad}$. The onset of absorption is at 3.35 eV as determined from the linear region on the Tauc plot in Figure 4.16(c) for the indirect band gap of brookite. The increased brookite reflectivity in the visible and NIR regions however are far enough from the band gap of any of the polymorphs to suggest that this difference in reflectivity is due to a difference in index of refraction.

A calculation of the index based on the fringe position and order gives us a measure of the order of the indices. From the specular measurement we know that the fringe near 405 nm is $m = 1$ and the thickness is roughly $d = 75\ nm$. We can estimate the position of the fringe for rutile (405 nm), anatase (403 nm), and for brookite (399 nm), and using the diffraction equation, $2d = m\lambda/n$, for normal incidence light we find the indicies of refraction in the violet to UV region for rutile ($n_{rutile} = 2.7$), anatase ($n_{anatase} = 2.68$), and brookite ($n_{brookite} = 2.66$). The index of refraction for rutile is in very good agreement with the ones reported elsewhere [56], which is most likely due to how close this data comes to the rutile band gap. However, the indices of refraction for anatase and brookite are switched, suggesting that the brookite band gap may be lower than that of anatase in qualitative agreement with the band gap ordering predicted by theory. To examine the band gap ordering in

more detail as well as the optical properties of the amorphous precursors we next examine the band gap as a function of film thickness before and after annealing.

4.3. Brookite Growth, and High Temperature Stability

The aim of this investigation is to evaluate the growth process and stability of brookite-containing thin films using in-situ optical microscopy and in-situ micro-Raman spectroscopy. A series of anneals are performed to evaluate the crystallization process from low temperature growth (275°C) to high temperature growth (400°C). This investigation documents some of the features of the nucleation and growth stages including nucleation rates, growth rates, and film morphology changes with annealing temperature. Once brookite is formed, high temperature anneals are performed and the film transformations (or lack thereof) are documented to investigate brookite stability. All films discussed in this section were deposited using 1 mTorr of oxygen pressure and a laser fluence of about 0.5 Jcm^{-2}, unless otherwise specified. This section begins with the in-situ growth of brookite, which is the first polymorph to form in these samples.

4.3.1. In-Situ Micro-Raman Spectroscopy and Optical Microscopy

Figure 4.18 shows the evolution of a high temperature (up to 400°C) anneal of a 65 nm thick TiO_2 film on a-SiO_2. After the anneal the different regions of the film were measured using Raman spectroscopy and were traced backwards in the video to their first appearance. Figure 4.18(a) shows the first appearances of brookite at 340°C. This is higher than the initial appearance of brookite in the in-situ XRD anneal shown in Figure 4.3(b) and the growth rate of the brookite regions is too fast to capture the first appearance of anatase. Once the sample is cooled the darker regions show clear Raman signatures of anatase, but the point at which the darker regions turn to anatase is not possible to determine in this video. One can track the number of brookite sites as a function of time/temperature and the brookite area fraction Figure 4.18(d) and Figure 4.18(e). Both the number of sites (black) and the area fraction (black) show the complex competition for material as the sample crystallizes, as indicated by the initial increase of sites/area followed by slowing down as the available amorphous material reaches zero.

Another interesting feature about this anneal is the rate of change in both the number of sites (gray) and the area fraction (gray) given in Figure 4.18(d) and Figure 4.18(e). The rates of change were obtained by first applying a linear interpolation to decrease the sample rate by a factor of 5 (need to decrease the overall error in the numerical differentiation). Then the numerical derivative is obtained by first accounting for the end points with the second order, forward and backward finite differences.

Then for the bulk of the data the fourth order central finite difference is used. After differentiation the data are then reduced back to the original sample rate and the results are shown in Figure 4.18(d) and Figure 4.18(e). The interesting features of the rates of change for the number of sites and the area fraction is the oscillatory behavior. These oscillations are a result of the growth and nucleation going through periods of activity followed by periods of rest. The growth rate and the nucleation rates are almost completely out of phase with each other as can be seen by the two rates indicating the global maximum in nucleation rate and the global maximum in growth rate, where when one is

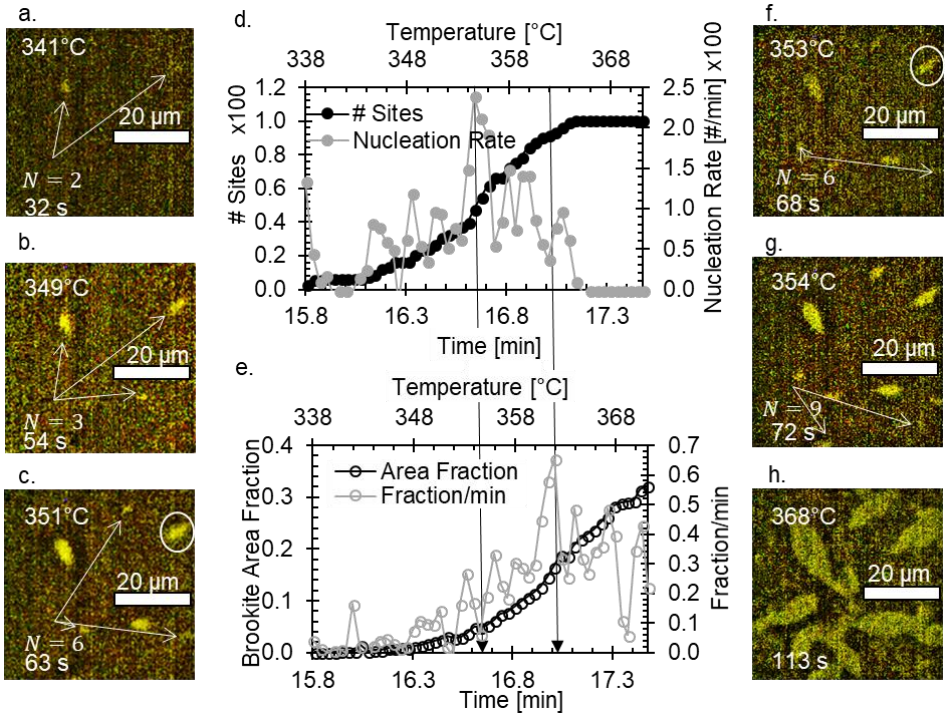

Figure 4.18: (a), (b), (c), (f), (g), and (h) x50 optical microscope snap shot images of brookite growing during a 400°C anneal. Temperature is displayed on the top left of each image, N is the number of events, and the time corresponds to the time since the appearance of the first events (roughly 15.8 minutes). (d) is the number of sites as a function of time and temperature (black) and the nucleation rate (gray). (e) is the brookite area fraction (black) and the area growth rate (gray).

maximum the other is at a minimum. Visually this oscillatory behavior is indicated in Figure 4.18(c) and Figure 4.18(f) by the sizes of the region indicated in the white circle.

Both the in-situ Optical Microscopy, Figure 4.18, and in-situ XRD, Figure 4.3(b), show that the initiation of brookite growth takes place at a lower temperature than 400°C, so a 62 nm thick section from the same deposition as the film in Figure 4.18 was annealed at 250°C, Figure 4.19. The sample was initially held at 250°C for 1 hour, after which only 2 nuclei were visible, each < 1 μm in diameter. Due to the minimal growth at 250°C, the temperature was increased to 275°C and held for an additional hour. As the time and temperature series of optical images show in Figure 4.19, only two small light dots are visible after initially increasing the temperature to 275°C, the brookite nuclei take about 25 minutes to grow to about 20 μm in length on their long growth axis (the black dots serve as fiducial marks for the analysis).

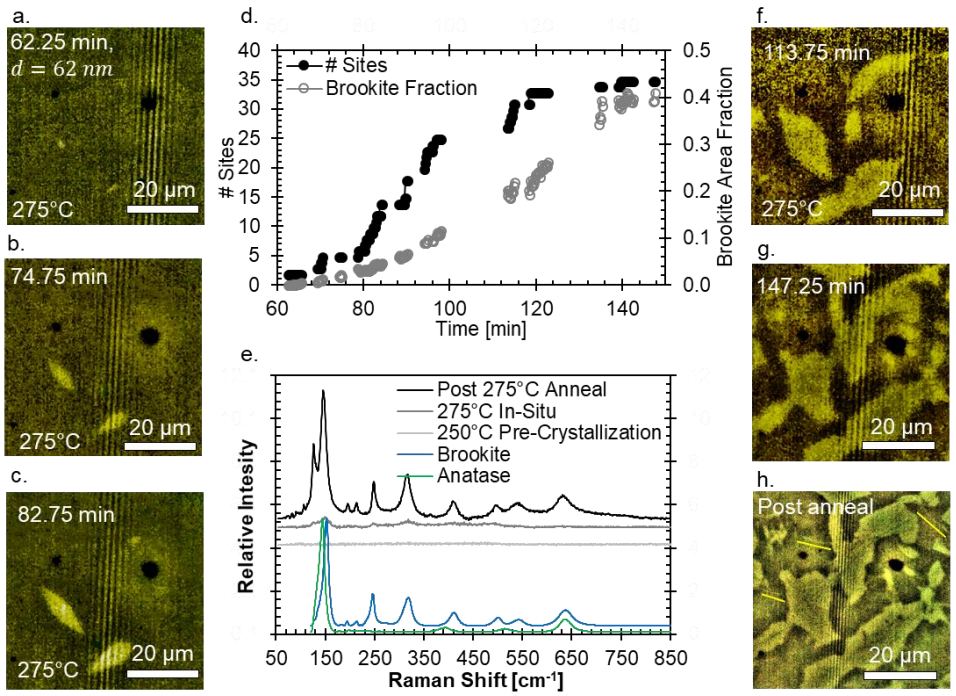

Figure 4.19: (a), (b), (c), (f), and (g) x50 optical microscope snap shot images of brookite growing during a 275°C anneal. Temperature is displayed on the bottom left of each image, and the time corresponds to the time in the top left is the time given in (d). (h) is a x100 magnification microscope image of the same section after cooling to room temperature. (d) is the number of sites(black) and the brookite area fraction (gray) as functions of time. (e) are the in-situ Raman spectra for the amorphous region at 250°C (light gray), a brookite region at 275°C (dark gray) and the same region after cooling (black). The reference spectra for brookite (blue, R050591) and anatase (green, R007058) are obtained from the RRUFF online database.

The slow growth rate at 275°C (6.8 nm/s for the long axis) compared to the 400°C anneal (20 nm/s for the long axis at the beginning), enables several new observations. First, Figure 4.19(d) shows that the number of sites/area fraction as a function of time are like those seen in the 400°C anneal in Figure 4.18. In both anneals the number of sites and the area fraction show a change in concavity as a function of time, indicating a slowing of the growth/nucleation as the amorphous material is converted to crystalline. Second, since the growth is slow enough, point Raman spectra can be obtained at temperature on isolated regions without interference from surrounding growing sites. Figure 4.19(e) shows three measurements taken at temperature (with brookite and anatase references in blue and green respectively), showing that most of the film at 250°C remains amorphous (light gray) with no indication of crystalline peaks. After increasing the temperature 275°C and measuring (dark gray) one of the brookite regions in Figure 4.19(b), small peaks belonging to the brookite structure are identifiable indicating that the brookite structure forms before any of the other polymorphs. Lastly, to verify the crystallinity of the brookite regions, after the sample is cooled and using the x100 microscope objective (to improve the resolution) the same brookite region is

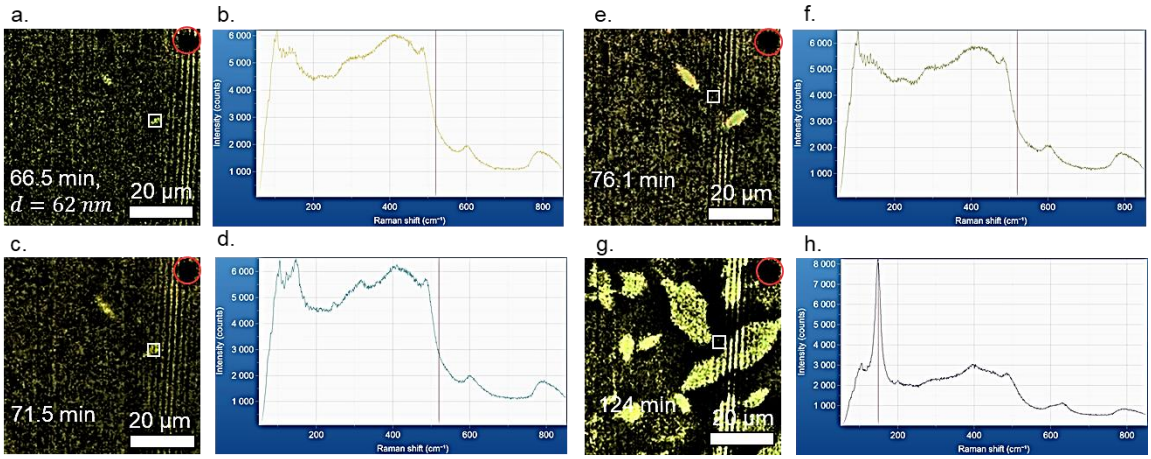

Figure 4.20: In-situ Raman measurements of brookite and anatase. The optical images are all x50 magnification and the red circles are of the fiducial debris used to orient the images for comparison. (a)-(b) Optical image and micro-Raman spectra for the small (~1μm) region inside the white box. (c)-(d) measurement of same spot as (a)-(b) roughly 5 minutes later. (d) shows that the light region inside the white box is large enough to show brookite character as seen by the 246 cm^{-1} and 318 cm^{-1} peaks. (e)-(f) Optical image and micro-Raman spectra for a spot between the two brookite regions. (f) shows the region in the white box is amorphous, especially when compared with (b) around 150 cm^{-1}. (g)-(h) Optical image and micro-Raman spectra for a spot close to the one in (e) about 1 hour later after the brookite regions are approaching merging, and still between the two brookite regions. (h) shows the Raman spectrum for the region in the white box in (g) indicating an anatase structure as seen by the peak at 150 cm^{-1} combined with the peak at 400 cm^{-1}. The peaks around 490 cm^{-1}, 600 cm^{-1}, and 800 cm^{-1} are all from the a-SiO_2 substrate.

measured and the black spectrum in Figure 4.19(e) is obtained showing the strong brookite character after annealing. Then to investigate the claim that brookite is the first polymorph to form some additional measurements are made of the region surrounding the brookite sites.

To investigate the crystallization competition, for the amorphous material, of anatase and brookite, two regions were tracked. Figure 4.20(a) and Figure 4.20(e) show the two regions (indicated by the white box) measured at 275°C, at the times indicated, one that show promise of growing into a larger brookite region and the other a spot between two brookite regions. Figure 4.20(a)-(d) show a measurement of the brookite region, while it is still small (~1 μm), where the 150 cm^{-1} Raman peak is the first to appear in Figure 4.20(b). Then in Figure 4.20(d), 5 minutes after the brookite site was first measured, the same spot is measured again and the unique brookite peaks at 250 cm^{-1} and 318 cm^{-1} are now clearly visible. Then approximately 10 minutes after the initial measurement of the small brookite region, Figure 4.20(e)-(f) show a measurement of the region between the two brookite sites. Figure 4.20(f) contains the Raman spectrum showing that the region around the brookite sites is still amorphous, 5 minutes after the brookite Raman signature is clearly defined. The amorphous character of this region can be seen more clearly when comparing Figure 4.20(f) with Figure 4.20(b) around 150 cm^{-1}, where the initial indications of crystallization are seen in Figure 4.20(b). Then about 1 hour later the region between the two brookite sites is measured again, as seen in Figure 4.20(g)-(h) showing that anatase is now present. This is seen in Figure 4.20(h) by the presence of the anatase 398 cm^{-1} peak combined with the higher intensity of the 148 cm^{-1} peak. Overall, Figure 4.20 shows that brookite crystallizes before anatase, however it does not show when the anatase forms or how it forms relative to the brookite regions.

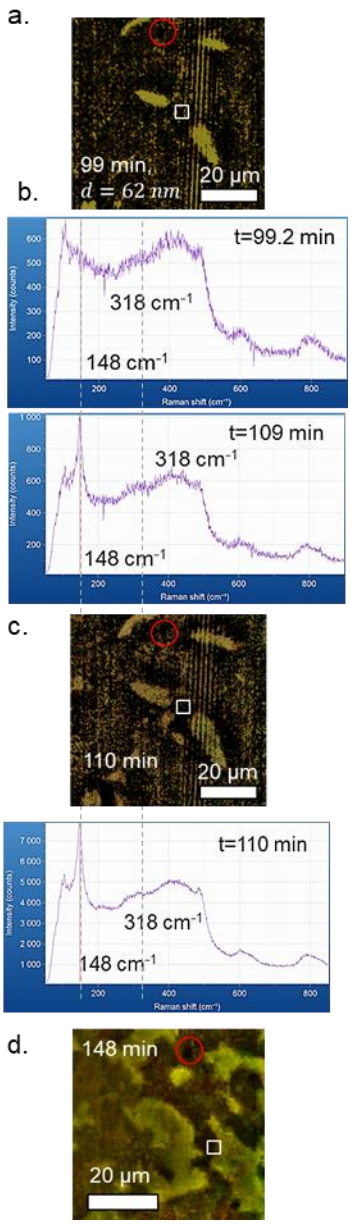

Figure 4.21: Raman Spectral evolution of amorphous to brookite transition. Red circles indicate fiducial debris for reference and white boxes indicate laser position and size.

To investigate the nucleation and growth of anatase, the Raman laser is positioned between two brookite sites, shown by the white box in Figure 4.21(a), and the Raman spectra are monitored in-situ. Since the orientation of the two brookite sites in Figure 4.21(a) suggests they will grow toward each other (confirmed by Figure 4.21(d)). The in-situ monitoring of the Raman spectra involves collecting photons for 5 seconds, recording the results, and then repeating. Since brookite is the first polymorph to grow, the in-situ Raman (Figure 4.21(b)) aims at identifying when anatase appears and if brookite aids in the nucleation and growth of the anatase regions. However, since the collection time is shorter for the in-situ Raman the signal to noise ratio is significantly lower than in a normal measurement but the growth of the peak at 148 cm^{-1} is still evident as the first peak to form in Figure 4.21(b) but is not sufficient to distinguish between brookite and anatase. A slight modification to the a-SiO_2 peak around 290 cm^{-1} is observable as well which may belong to either the brookite B_{1g} vibrational mode at 283 cm^{-1} or the B_{3g} mode at 318 cm^{-1} during formation. To confirm this spectrum is related to brookite (and not anatase), without moving the laser a complete scan is obtained just after the in-situ monitoring Figure 4.21(c) and shows a clear signature of the brookite 318 cm^{-1} peak. The in-situ monitoring of the amorphous film transforming directly into brookite does not conclusively show that anatase growth is independent of brookite. For instance, the identification of anatase between the two brookite sites in Figure 4.20(g), with the two long brookite growth direction perpendicular, may suggest that anatase prefers the sides of the brookite sites with lower curvature. Additional in-situ anneals are needed to determine when the anatase forms during the formation of brookite and where the anatase forms. Let us now turn to

examining the post anneal morphology of the films as there are some interesting features, such as brookite wisps and brookite veins, suggestive of the way brookite grows.

4.3.2. Post-Anneal Brookite Morphology

There are a few interesting features observed in-situ that are difficult to measure during an anneal as the film is constantly evolving and the resolving power of the x50 microscope object cannot resolve all the small changes in the film. The first is the effect on the film morphology with increasing annealing temperature. The second are smaller structures that appear within brookite regions (colloquially termed "veins") or between brookite regions ("wisps").

Morphological changes: Figure 4.22 shows a series of films post anneal, all annealed in-situ, and corresponding Raman spectra of the brookite portion of the film. Figure 4.22(a)-(c) show the x100 magnification optical microscope images of films annealed up to a maximum temperature of 275°C, 340°C, and 400°C respectively. These anneals were done on different sections of the same deposition, and thus all have the same amorphous precursor history. The most visually striking feature this series of anneals exhibits is that as the annealing temperature is decreased the brookite regions appear less broken up and dispersed. This is seen by the additional small white spots scattered throughout the anatase regions between brookite sites for the higher temperature anneals in Figure 4.22(b)-(c), and the lack thereof in the lower temperature anneal Figure 4.22(a). The small regions do show weak brookite Raman signatures but due to their size the spectra tend to be overshadowed by the intense anatase peaks. Next, the Raman spectra in Figure 4.22(d) show single point Raman spectra from the laser spots (green dots inside black circles) shown in Figure 4.22(a)-(c) all within a

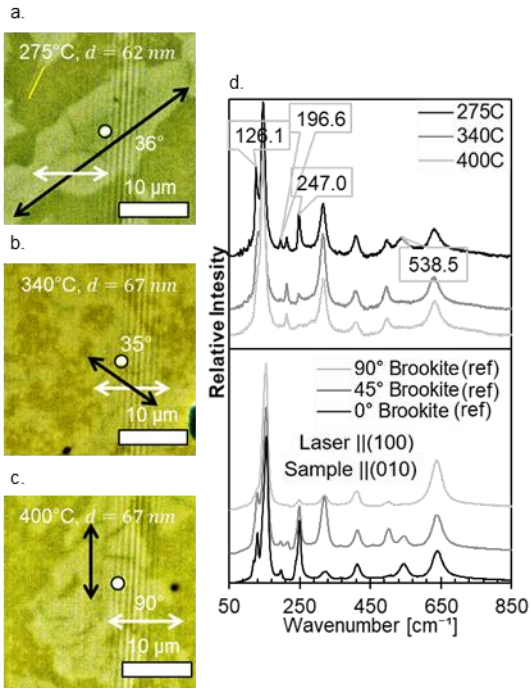

Figure 4.22: (a), (b), and (c) post-anneal x100 microscope images of samples annealed in-situ up to the given maximum temperature. (d) point-Raman spectra of the spot inside the black circle in (a), (b), and (c). The white arrow in the images indicates the laser polarization, while the black arrow indicates the major growth direction for the brookite region measured.

lighter brookite region. The Raman peaks labeled in Figure 4.22(d) are the peaks which are seen to change intensity the most with each sample. The brookite peaks identified (126 cm^{-1}, 196 cm^{-1}, 247 cm^{-1}, and 538 cm^{-1}) are all A_{1g} vibration modes for brookite, and all are documented as having strong dependences on laser polarization [76]. Furthermore, this polarization dependence is seen in the reference spectra Figure 4.22(d) from the RRUFF database (RRUFFID = R050591). In the reference spectra, the laser polarization is aligned in the (100) direction and the fiducial mark on the sample is aligned in the (010) direction. The angle for each measurement in the references refers to the orientation of the laser polarization relative to the fiducial mark. In Figure 4.22(a)-(c), to emphasize the dependence of the spectra on the laser polarization, the direction of the natural polarization (no polarizers used) of the laser is indicated by the white arrow (horizontal for all measurements) and the major growth direction for the brookite site is indicated by the black arrow along with the smallest angle between the laser polarization and the long growth direction. This shows that the likely reason for the variation in the Raman peaks from sample to sample is due to the orientation of the major growth direction with respect to the laser polarization.

Veins: One feature common amongst all the images of brookite regions in Figure 4.22 is the dark grey lines that divide the brookite regions, like veins in a leaf. To investigate the veins further, a 2D

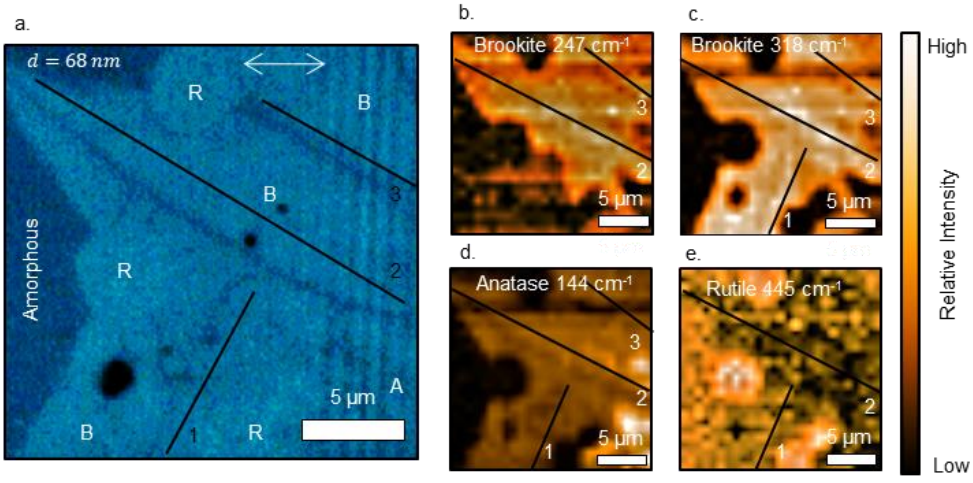

Figure 4.23: 2D Micro-Raman map of 400°C annealed sample. (a) x100 microscope image of brookite region containing multiple brookite veins. The 3 most prominent veins are labeled 1-3 for reference in the Raman maps. (b), (c), (d), and (e) are intensity maps of the Raman spectra taken across the image in (a). Each Raman intensity map is centered on the given polymorph peak and the vein-like structure can be seen in each map as a decrease in Raman intensity.

Raman map is constructed across a section of film containing multiple veins, Figure 4.23. The x100 microscope image in (a) shows the morphology of the sample corresponding to the Raman maps shown in Figure 4.23(b)-(e). The most prominent veins in Figure 4.23(a) are indicated with a black line and numbered 1-3. 2D-Raman intensity maps for the four polymorph peaks (B 246 cm^{-1}, B 318 cm^{-1}, A 144 cm^{-1}, and R 445 cm^{-1} within ±5 cm^{-1}) show that the lighter regions in Figure 4.23(a) are brookite, the darkest regions are amorphous, circular (bubble) regions are rutile, and there is a small anatase section in the bottom right of the image. The veins numbered 2 and 3 are evident in the maps of the two brookite peaks as lines of decreased intensity, whereas the vein labeled 1 does not show up in the map of the brookite 246 cm^{-1}. The reason vein 1 is not visible is that the polarization of the laser for these measurements is almost perpendicular to the vein (like the spectrum obtained for the measurement of the brookite in Figure 4.22(c)), suggesting this image is at the merge point for two different brookite nuclei, with perpendicular long axis growth direction. This further confirms the polarization dependence of the brookite regions with respect to the polarization of the laser.

Furthermore, the combination of lower Raman intensity for the veins in the brookite map, the lack of intensity of the veins in the other polymorph peak maps, and the optical contrast similarity of the veins with the amorphous sections suggests the veins are a form of amorphous TiO_2. However, since the veins are pinned between two brookite regions it is likely the veins are not the same type of amorphous as the larger amorphous regions. Additionally, Figure 4.19(h) shows multiple brookite sites that merged during annealing and are connected via the same vein (post anneal), as opposed to separated by a vein, as if pinned between two sites from merging. Thus, the veins must be a part of either the growth of brookite or the solidification of the crystal structure during cooling.

Wisps: The next interesting feature observed during the in-situ annealing is the formation of brookite colored lines penetrating through the amorphous/anatase regions, like tendrils or wisp. Some examples of these wisps are indicated by yellow lines in Figure 4.19 and Figure 4.22. Figure 4.24 consists of a series of images taken on the same section of film after annealing up to 400°C and showing the presence of a wisp structure. The wisp in the x100 magnification optical image in Figure 4.24(a) corresponds to the light region indicated by the yellow arrow. For reference the laser spot is

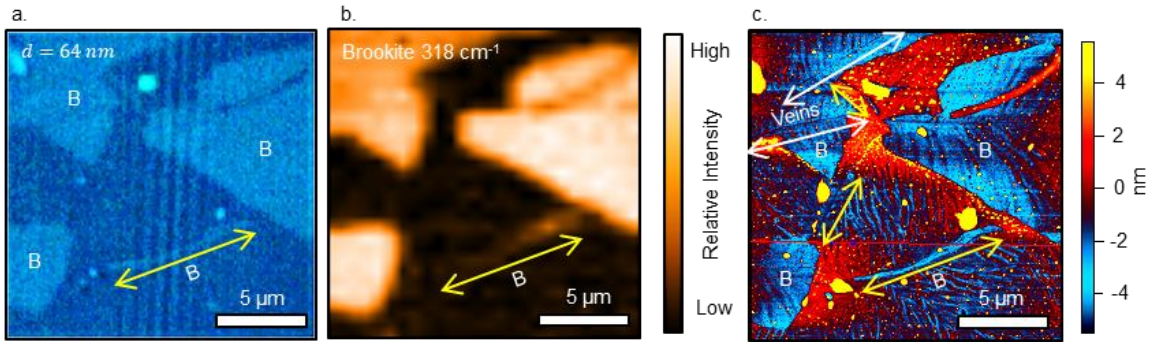

Figure 4.24: (a) x100 optical microscope image of a 400°C annealed sample. (b) 2D Micro-Raman map with the intensity for the brookite 318 cm^{-1} peak ±5 cm^{-1}. The bright yellow regions indicate where the brookite sections are within the optical microscope image in (a). (c) AFM map of the same region in (a) and (b). Yellow arrows indicate brookite wisps, white arrows indicate veins, and the sections labeled B are identified by the Raman intensity map as brookite.

also included in this image, top middle (green spot), showing that the width of the wisp is about half the diameter of the laser spot, <1 µm. Figure 4.24(b) shows the 2D Raman map for the brookite 318 cm^{-1} (±5 cm^{-1}) peak, with the brightest yellow sections indicating the higher intensity of the brookite peak in that region. As with the optical microscope image, the wisp is observable in the Raman map (yellow arrow), confirming the optical microscope identification of these wisps as brookite.

The atomic force microscope (AFM) image, Figure 4.24(c) shows some things that were not visible in the optical microscope image or the Raman map. The AFM image (tapping mode with 51.2 lines/µm) combined with the information from the in-situ and 2D Raman maps hint at the way in which brookite forms. First, brookite veins are visible in the AFM image that were not seen in the optical microscope, along with additional fissures emanating from the central wisp. The AFM images suggest that these wisps form as crevices, about 4-5 nm deep in the film, which is the same depth at which the larger brookite regions are observed. However, without better resolution it is not possible to determine if the fissures appear because of the wisps or vice versa, but by comparing the brookite wisps and the fissures relative to the larger brookite section it may seem plausible that this film was in the process of growing additional brookite when it was quenched. Though additional anneals with higher resolution are needed to observe the formation of the wisps and the fissures.

4.3.3. High Temperature Polymorph Stability

In this section, the high temperature stability of samples containing brookite, anatase, and rutile is investigated. Since previous reports of the transition of brookite to rutile suggest the temperature range 500-600°C [77], the first test performed on a high fraction brookite sample is done at 600°C. After the 600°C anneal, little change in the film morphology and crystallinity is observed and so another high fraction brookite sample is annealed at 700°C.

600°C anneal: Figure 4.25(a), post 400°C anneal, and Figure 4.25 (b), post 600°C anneal, show the visually minimal morphological change in a high fraction brookite film annealed for 25.25 hours at 600°C under ambient atmosphere. The observable visual changes include a darkening of the veins, the formation of additional veins, and a decreased contrast between the brookite, anatase, and rutile regions, labeled A, B, and R. The boxes in Figure 4.25(b) correspond to the positions of the laser for the measurements in the comparison of the Raman spectra in Figure 4.25(c) (black box goes with black spectrum and white box goes with light gray spectrum). The two boxes are both within about 1 μm[3] of each other. The anatase: brookite mixed nature of this section of film is evident from the anatase peaks at 394 cm^{-1} and 514 cm^{-1} (though not for the 15 minute anneal) and the brookite peaks at 247 cm^{-1}, 318 cm^{-1} (seen in all

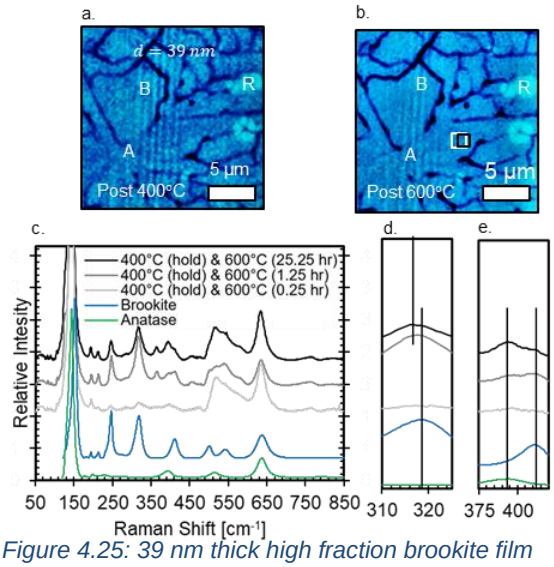

Figure 4.25: 39 nm thick high fraction brookite film initially annealed with the 400°C hold RTA profile(a), then annealed in the oven at 600°C for 15 minutes, 1 hour, and lastly 24 hours (b) all at ambient atmosphere. (a) and (b) are both x100 magnification images. The black and white boxes in (b) indicate the position of the laser during two of the measurements. (c) the Raman spectra of the same spot measured after each anneal (d) is the same data as (c) but zoomed into the brookite 318 cm^{-1} peak. (e) the Raman spectra centered on the anatase 394 cm^{-1} peak. The shift in these peaks as a function of annealing time is within the experimental uncertainty (± 3 cm^{-1}) for this measurement.

[3] Roughly the diameter of the laser spot

spectra), and the rarely seen 366 cm^{-1}. The rarely seen 366 cm^{-1} peak of brookite is a B_{2g} vibrational mode and appears strongest when the laser and scattered light are aligned perpendicular to each other (laser oriented in the X direction and scattered light oriented in the Z direction) [78]. Figure 4.25(d)-(e) show additionally no significant shifting of either the brookite or anatase peaks indicating very little change to the strain on the crystal structure [79]. Lastly, by considering the brookite 318 cm^{-1} as a function of annealing time we can see that after the initial 1 hour of annealing the peak width shows very little change (even though the peak intensity increases). However, further annealing for an additional 24 hours shows an increase in the peak width suggestive of a decrease in crystallinity [80]. This same trend is also observable for the brookite 246 cm^{-1} peak, though for both peaks this is only a slight change and does not show quantitatively and large changes in crystallinity. The high fraction brookite film annealed at 600°C did not change morphology and there was no large polymorphic transformation to anatase or rutile.

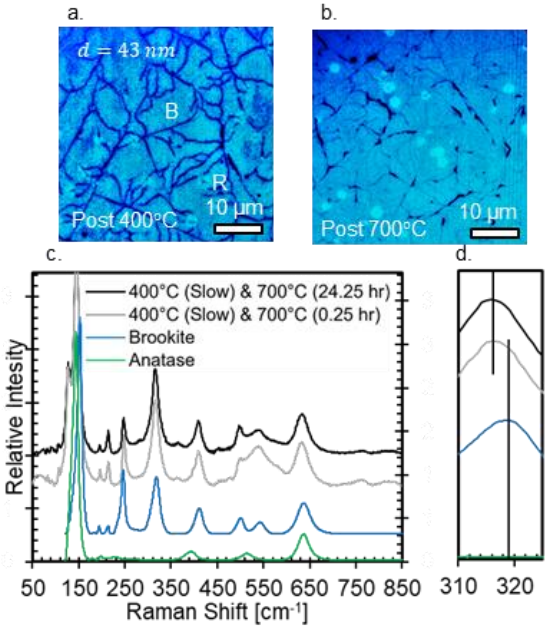

Figure 4.26: 43 nm thick high fraction brookite film initially annealed with the 400°C slow RTA profile, then annealed in the oven at 700°C for 15 minutes (a), then 24 hours (b) at ambient atmosphere. (a) and (b) are both x100 magnification images. (c) the Raman spectra of similar regions measured after the all anneals. (d) is the same data as (c) but zoomed into the brookite 318 cm^{-1} peak. The shift in these peaks as a function of annealing time is within the experimental uncertainty (± 3 cm^{-1}) for this measurement.

700°C anneal: Figure 4.26 shows the optical images and Raman spectra of a second high-fraction brookite film before and after annealing at 700°C. As can be seen from Figure 4.26 (a)-(b), before the 700°C anneal (a) the brookite veins are clearly defined, however after the 700°C anneal (b) most of the veins are decreased in contrast suggesting a transformation of the amorphous veins. The drastic decrease in the contrast in the veins is the reason why the two images are not of the same section, as the original position could not be found. While the position of the laser for the two measurements in Figure 4.26(c) is different, the positions were chosen as representative and show that with the increased annealing time, a similar

result to the anneal in Figure 4.25 is obtained. Figure 4.26(d) features the brookite 318 cm^{-1} peak which shows minimal shift in the peak position for this mode, a shift which still puts the peak position within the experimental uncertainty of the reference position.

The fact that brookite is the first polymorph to form during the in-situ anneals is very suggestive of Oswald's Rule of stages, where intermediate metastable phases form first during crystallization, prior to formation of the stable phase [81]. The final morphology observed in brookite containing films after annealing looks like those observed during phase separation of polymer thin films [82] in both scale and morphological variation. However, upon further thermal treatment, Sun and Ceder [52] suggest that the polymorph with the lowest energy (anatase), or the ground state structure (rutile), should consume the higher energy metastable brookite structure, but we find instead that the mixed brookite/anatase structure is minimally perturbed by additional heat treatments applied for as long as 24 hours.

5. Conclusion

In this work we combined theory with synthesis and characterization of TiO_2 thin films that are amorphous as deposited, and subsequently annealed to form one or another of several polymorphs. We identify the deposition/annealing conditions ($0.25 < \langle v_d \rangle < 0.65$ Å$/s, 0.5 < P_d < 1.0\ mTorr$, and $T_{max} < 400$℃) necessary to produce high-fraction, metastable brookite. In collaboration with theorists at MIT we show that through DFT calculations, allowing for the incorporation of various Na defects into the TiO_2 matrix (through either Na-ion defects or Na_2O_3 incorporation), the brookite structure is never the most stable polymorph when combined with sodium. To show experimentally that Na is not needed to stabilize brookite we, in collaboration with SLAC and CSM, show that brookite can be synthesized on substrates such as fused silica, which contain zero sodium. After showing that brookite is synthesizable via PLD, without the use of any of the most common helper ions, we further investigate modification to the amorphous precursor and the subsequent growth of brookite.

Monitoring the unique brookite (211) and anatase (101) diffraction peaks using in-situ XRD we find that brookite and anatase crystallize simultaneously around 280°C while heating up to 400°C. However, while monitoring the in-situ progression of brookite regions in an optical microscope we show that when held at 250°C, brookite is the first polymorph to form, before anatase or rutile, and is followed by growth of anatase. Assuming that rutile is the ground state structure for the system this ordering of polymorph formation is very suggestive of Oswald's rule of stages where the least stable phase is the first one formed during crystallization. Ultimately, changing the annealing conditions did not alter the fraction of brookite within the final product.

This suggests that modifications to the amorphous precursor via deposition rate or oxygen content changes the nucleation barriers for the different polymorphs, giving rise to brookite formation for film thicknesses of (45-65 nm) with deposition rates (0.25-0.65 Å/s) or with deposition oxygen pressures of 0.5-1.0 mTorr. However, anatase appearing later and more rapidly than brookite during the anneal suggests that it has a "kinetic advantage of heterogeneous nucleation on pre-existing metastable phases" [52]. It is likely that anatase nucleates on the brookite surfaces.

In our investigation of the morphological structure and features observed during growth of the three different polymorphs, a few trends emerged. First, the identification of veins within the brookite structure are observed to correlate with strain, with fewer veins appearing in less strained brookite films. Further investigation of the veins is needed to quantify the nature of this strain and how it relates to the growth of brookite. Next, brookite wisps that appear during annealing suggest that during later stages of growth brookite creates cervices in the surface of the film directed toward other brookite regions for them to eventually merge together. Then lastly, modifications to the amorphous precursor during deposition either through adjusting the growth rate or adjusting the oxygen pressure is an effective method for producing high-fraction brookite thin films on amorphous substrates.

6. Works Cited

[1] K. H. e. a. Stone, "Influence of amorphous structure on polymorphism in vanadia," *APL Mater.,* vol. 4, p. 076103, 2016.

[2] Y. e. a. Chimupala, "Synthesis and characterization of mixed phase anatase TiO2 and sodium-doped TiO2(B) thin films by low pressure chemical vapour deposition (LPCVD)," *RSC Adv.,* vol. 4, p. 48507, (2014).

[3] D. Rudmann, D. Brémaud, H. Zogg and A. N. Tiwari, "Na incorporation into Cu(In,Ga)Se2 for high-efficiency flexible solar cells on polymer foils," *J. App. Phys.,* vol. 97, p. 084903, (2005).

[4] A. e. a. Rockett, "Na in selenized Cu(In,Ga)Se2 on Na-containing and Na-free glasses: distribution, grain structure, and device performances," *Thin Solid Films,* vol. 372, pp. 212-217, (2000).

[5] V. I. Keesmann, "Zur hydrothermalen Synthese von Brookit," *Zeit. anorg. allge. Chemie. Band.,* vol. 346, pp. 30-43, (1966).

[6] M. Cargnello, T. R. Gordon and C. B. Murray, "Solution-Phase Synthesis of Titanium Dioxide Nanoparticles and Nanocrystals," *Chem. Rev.,* vol. 114, pp. 9319-9345, 2014.

[7] M. P. F. A. G. Filler, "The History, Development and Impact of Computed Imaging in Neurological Diagnosis and Neurosurgery: CT, MRI, and DTI," *Nature Precedings,* 2009.

[8] V. Stevanović, "Sampling Polymorphs of Ionic Solids using Random Superlattices," *Phys. Rev. Lett.,* vol. 116, pp. 075503-1-5, 2016.

[9] M. Aykol, S. S. Dwaraknath, W. Sun and K. A. Persson, "Thermodynamic limit for synthesis of metastable inorganic materials," *Sci. Adv.,* vol. 4, 2018.

[10] Q. Liu, N. Zhang, F. Liu and Z. Liu, "Structural, elastic, electronic and optical properties of various mineral phases of TiO2 from first-principles calculations," *Phys. Scr.,* vol. 89, p. 075703, (2014).

[11] J. e. a. Buckeridge, "Polymorph Engineering of TiO2: Demonstrating How Absolute Reference Potentials Are Determined by Local Coordination," *Chem. Mater.,* vol. 27, pp. 3644-3851, (2015).

[12] D. A. H. Hanaor and C. C. Sorrell, "Review of the anatase to rutile phase transformation," *J. Mater. Sci.,* vol. 46, pp. 855-874, 2011.

[13] X. Chen and S. S. Mao, "Titanium Dioxide Nanomaterials: Synthesis, Properties, Modifications, and," *Chem. Rev.,* vol. 107, no. 7, pp. 2891-2959, (2007).

[14] A. B. Di Paola and L. Palmisano, "Brookite, the least known TiO2 photocatalyst," *Catalysts,* vol. 3, pp. 36-73, 2013.

[15] T. Balaganapathi, B. KaniAmuthan, S. Vinoth and P. Thilakan, "Synthesis, characterization and dye adsorption studies of porous brookite and mixed brookite with rutile TiO2 using PEG assisted sol-gel synthesis process," *Mater. Res. Bull.,* vol. 91, pp. 114-121, (2017).

[16] J. J. M. e. a. Vequizo, "Trapping-Induced Enhancement of Photocatalytic Activity on Brookite TiO2 Powders: Comparison with Anatase and Rutile TiO2 Powders," *ACS Catalysis,* vol. 7, pp. 2644-2651, (2017).

[17] H. e. a. Lin, "Synthesis of High-Quality Brookite TiO2 Single-Crystalline Nanosheets with Specific Facets Exposed: Tuning Catalysts from Inert to Highly Reactive," *J. Amer. Chem. Soc.,* vol. 134, pp. 8328-8331, (2012).

[18] M. Jansen, "A Concept for Synthesis Planning in Solid-State Chemistry," *Ang. Chem. Inter. Ed.,* pp. 3746-3766, (2002).

[19] M. R. e. a. Ranade, "Energetics of nanocrystalline TiO2," in *Proceedings of the National Academy of Sciences of the United States of America*, (2002).

[20] J. e. a. Baumgartner, "Nucleation and growth of magnetite from solution," *Nature Mat.,* vol. 12, pp. 310-314, (2013).

[21] J. Sun, A. Ruzsinszky and J. P. Perdew, "Strongly Constrained and Appropriately Normed Semilocal Density Functional," *Phys. Rev. Lett.,* vol. 115, no. 3, p. 036402, (2015).

[22] D. A. Kitchaev, S. T. Dacek, W. Sun and G. Ceder, "Thermodynamics of Phase Selection in MnO2 Framework Structures through Alkali Intercalation and Hydration," *J. Am. Chem. Soc.,* vol. 139, pp. 2672-2681, (2017).

[23] D. A. Kitchaev and G. Ceder, "Evaluating structure selection in the hydrothermal growth of FeS2 pyrite and marcasite," *Nature Comm.,* (2016).

[24] W. Sun, S. Dacek, S. Ong, G. Hautier, A. Jain, W. Richards, A. Gamst, K. Persson and G. Ceder, "The thermodynamic scale of inorganic crystalline metastability.," *Sci. Adv.,* vol. 2, no. 11, 2016.

[25] J. J. e. a. De Yoreo, "Crystallization by particle attachment in synthetic, biogenic, and geologic environments," *Science,* vol. 349, no. 6247, (2015).

[26] D. Kim, W. Kim, S. Kim and S. Hong, "Brookite TiO2 Thin Film Epitaxially Grown on (110) YSZ Substrate by," *Appl. Mater. Inter.,* vol. 6, pp. 11817-11822, (2014).

[27] M. G. e. a. Manera, "Enhancement of the optically activated NO2 gas sensing response of brookite TiO2 nanorods/nanoparticles thin films deposited by matrix-assisted pulsed-laser evaporation," *Sensors and Actuators B,* vol. 161, pp. 869-879, (2012).

[28] W. e. a. Wang, "Synthesis and characterization of structural and optical properties of heteroepitaxial brookite TiO2 single crystalline films," *Scr. Mater.,* vol. 115, pp. 75-79, (2016).

[29] K. Srivatsa, "Pure brookite titania crystals with large surface area deposited by Plasma Enhanced Chemical Vapour Deposition Technique," *Thin Solid Films,* vol. 515, no. 21, p. 7443–7446, (2008).

[30] V. e. a. Swamy, "Finite-size and pressure effects on the Raman spectrum of nanocrystalline anatase TiO2," *Phys. Rev. B,* vol. 71, p. 184302, (2005).

[31] R. e. a. Buonsanti, "Nonhydrolytic Synthesis of High-Quality Anisotropically Shaped Brookite TiO2 Nanocrystals," *J. Am. Chem. Soc.,* vol. 130, pp. 11223-11233, (2008).

[32] H. Zhang and J. F. Banfield, "Understanding Polymorphic Phase Transformation Behavior during Growth of Nanocrystalline Aggregates: Insights from TiO2," *J. Phys. Chem. B,* vol. 104, pp. 3481-3487, (2000).

[33] R. L. Penn and J. F. Banfield, "Oriented attachment and growth, twinning, polytypism, and formation of metastable phases: Insights from nanocrystalline TiO2," *Am. Min.,* vol. 83, pp. 1077-1082, (1998).

[34] I. N. Kuznetsova, V. Blaskov, I. Stambolova, L. Znaidi and A. Kanaev, "TiO2 pure phase brookite with preferred orientation synthesized as a spin-coated film," *Mater. Lett.,* vol. 59, pp. 3820-3823, (2005).

[35] A. Pottier, C. Chanéac, E. Tronc, L. Mazerolles and J. Jolivet, "Synthesis of brookite TiO2 nanoparticles by thermolysis of TiCl4 in strongly acidic aqueous media," *J. Mater. Chem.,* vol. 11, pp. 1116-1121, (2001).

[36] X. Bokhimi, "Local order in titania polymorphs," *Int. J. Hydro. Engy.,* p. 1279–1287, (2001).

[37] M. P. Moret, R. Zallen, D. P. Vijay and S. B. Desu, "Brookite-rich titania films made by pulsed laser deposition," *Thin Solid Films,* vol. 366, pp. 8-10, (2000).

[38] A. K. Sharma, R. K. Thareja, U. Willer and W. Schade, "Phase transformation in room temperature pulsed laser deposited TiO2 thin films," *App. Sur. Sci.,* vol. 206, pp. 137-148, (2003).

[39] S. P. Ong, L. Wan, B. Kang and G. Ceder, "Li-Fe-P-O2 Phase Diagram from First Principles Calculations.," *Chem. Mater.,* vol. 20, no. 5, p. 1798–1807, 2008.

[40] A. Jain, G. Hautier, S. P. Ong, C. Moore, C. Fischer, K. Persson and G. Ceder., "Formation enthalpies by mixing GGA and GGA + U calculations.," *Phys. Rev. B,* vol. 84, no. 4, p. 045115, 2011.

[41] A. M. e. a. Alotaibi, "Chemical Vapor Deposition of Photocatalytically Active Pure Brookite TiO2 Thin Films," *Chem. Mater.,* vol. 30, pp. 1353-1361, 2018.

[42] M. Curnan and J. Kitchin, "Investigating the Energetic Ordering of Stable and Metastable TiO2 Polymorphs Using DFT plus U and Hybrid Functionals," *J. Phys. Chem. C,* vol. 119, no. 36, pp. 21060-21071, 2015.

[43] J. Trail, B. Monserrat, P. L. Rıos, R. Maezono and R. J. Needs, "Quantum Monte Carlo study of the energetics of the rutile, anatase, brookite, and columbite TiO 2 polymorphs," *Phys. Rev. B,* vol. 95, no. 12, 2017.

[44] J. e. a. Haggerty, "High-fraction brookite films from amorphous precursors," *Sci Rep,* vol. 7, no. 15232, 2017.

[45] S. O'Leary, S. Johnson and P. Lim, "The relationship between the distribution of electronic states and the optical absorption spectrum of an amorphous semiconductor: An empirical analysis," *J. App. Phys.,* vol. 82, p. 3334, 1997.

[46] B. Lafuente, R. T. Downs, H. Yang and N. Stone, The power of databases: the RRUFF project., Thomas Armbruster, Rosa Micaela Danisi (Eds.): De Gruyter, (2015).

[47] B. H. Toby and R. B. Von Dreele, "GSAS-II: the genesis of a modern open-source all purpose crystallography software package," *J. App. Crys.,* vol. 46, no. 2, pp. 544-549, (2013).

[48] J. e. a. Bednarcik, "In situ XRD studies of nanocrystallization of Fe-based metallic glass: a comparative study by reciprocal and direct space methods," *Phys. Chem. Chem. Phys.,* vol. 15, no. 22, pp. 8443-8846, 2013.

[49] L. A. Giannuzzi and F. A. Stevie, "A review of focused ion beam milling techniques for TEM specimen preparation," *Micron,* vol. 30, pp. 197-204, 1999.

[50] G. Kresse and J. Furthmuller, "Efficient iterative schemes for ab initio total-energy calculations using a plane-wave basis set," *Phys. Rev. B,* vol. 54, no. 16, pp. 11169-11186, (1996).

[51] G. Kresse and D. Joubert, "From ultrasoft pseudopotentials to the projector augmented-wave method," *Phys. Rev. B,* vol. 59, no. 3, pp. 1758-1775, (1999).

[52] W. Sun and G. Ceder, "Induction time of a polymorphic transformation," *CrystEngComm,* vol. 19, pp. 4576-4585, 2017.

[53] A. Belsky, M. Hellenbrandt, V. L. Karen and P. Luksch, "New developments in the Inorganic Crystal Structure Database (ICSD): accessibility in support of materials research and design," *Acta Cryst.,* vol. B58, pp. 364-369, 2002.

[54] W. Sun, S. Jayaraman, W. Chen, K. Persson and G. Ceder, "Nucleation of metastable aragonite CaCO3 in seawater.," *Proc. Nat. Acad. Sci. U.S.A.,* vol. 112, no. 11, pp. 199-3204, 2015.

[55] M. Nielsen, S. Aloni and J. De Yoreo, "In situ TEM imaging of CaCO3 nucleation reveals coexistence of direct and indirect pathways," *Scinece,* vol. 345, no. 6201, pp. 1158-1162, 2014.

[56] X. Rocquefelte, F. Goubin, H. Koo, M. Whangbo and S. Jobic, "Investigation of the Origin of the Empirical Relationship between Refractive Index and Density on the Basis of First Principles Calculations for the Refractive Indices of Various TiO2 Phases," *Inorg. Chem.,* vol. 43, pp. 2246-2251, (2004).

[57] M. N. Rahaman, "Grain Growth and Microstructure Control," in *Ceramic Processing and Sintering*, Boca Raton, Fl, CRC Press, (2003), pp. 540-619.

[58] M. R. R. Vaziri, F. Hajiesmaeilbaigi and M. H. Maleki, "Monte Carlo simulation of the subsurface growth mode during pulsed laser deposition," *J. App. Phys.,* vol. 110, p. 043304, 2011.

[59] M. Strikovski and J. H. Miller, "Pulsed laser deposition of oxides: Why the optimum rate is about 1 Å per pulse," *App. Phys. Lett.,* vol. 73, 1998.

[60] A. Gupta, "Gas-phase oxidation chemistry during pulsed laser deposition of YBa2Cu307S films," *J. App. Phys.,* vol. 73, no. 11, p. 7877, 1993.

[61] S. Lee, T. L. Meyer, S. Park, T. Egami and H. N. Lee, "Growth control of the oxidation state in vanadium oxide thin films," *App. Phys. Lett.,* vol. 105, p. 223515, 2014.

[62] D. G. e. a. Syarif, "Preparation of anatase and rutile thin films by controlling oxygen partial pressure," *App. Sur. Sci.,* vol. 193, pp. 287-292, 2002.

[63] M. e. a. Horprathum, "Oxygen Partial Pressure Dependence of the Properties of TiO2 Thin Films Deposited by DC Reactive Magnetron Sputtering," *Proc. Eng.,* vol. 32, pp. 676-682, 2012.

[64] H. e. a. Long, "Growth and characteristics of laser deposited anatase and rutile TiO2 films on Si substrates," *Thin Solid Films,* vol. 517, pp. 745-749, 2008.

[65] M. e. a. Morita, "Growth of native oxide on a sincon surface," *J. App. Phys.,* vol. 68, no. 3, 1990.

[66] G. Lu, S. L. Bernasek and J. Schwartz, "Oxidation of a polycrystalline titanium surface by oxygen and water," *Sur. Sci.,* vol. 458, pp. 80-90, 2000.

[67] G. Balakrishnan, V. R. Bandi, S. Rajeswari, N. Balamurugan, R. V. Babu and J. Song, "Effect of oxygen partial pressure on microstructural and optical properties of titanium oxide thin films prepared by pulsed laser deposition," *Mat. Res. Bull.,* vol. 48, pp. 4901-4906, 2013.

[68] S. Waseem, S. Anjum, L. Mustafa, A. Dar, F. Bashir and R. Zia, "Effects of Cr and Fe co-doping on structural, optical, electrical and magnetic properties of titanium dioxide (TiO2)," *Mater. Sci. Poland,* vol. 33, no. 3, pp. 508-514, 2015.

[69] D. Reyes-Coronado, G. Rodr´ıguez-Gattorno, M. E. Espinosa-Pesqueira, C. Cab, R. d. Coss and G. Oskam, "Phase-pure TiO2 nanoparticles: anatase, brookite and rutile," *Nanotechnology,* vol. 19, p. 145605, 2008.

[70] D. Komaraiah, P. Madhukar, Y. Vijayakumar, M. Reddy, V. Ramana and R. Sayanna, "Photocatalytic degradation study of methylene blue by brookite TiO2 thin film under visible light irradiation," *Mater. Today: Proc.,* vol. 3, no. 10, p. 3770–3778, 2016.

[71] M. Koelsch, S. Cassaignon, J. Guillemoles and .. Jolivet, "Comparison of optical and electrochemical properties of anatase and brookite TiO2 synthesized by the sol–gel method," *Thin Solid Films,* Vols. 403-404, pp. 312-319, 2002.

[72] S. Yamamoto, T. Sumita, Sugiharuto, A. Miyashita and H. Naramoto, "Preparation of epitaxial TiO2 films by pulsed laser deposition technique," *Thin Solid Films,* vol. 401, pp. 88-93, 2001.

[73] B. Zhao, J. Zhou, Y. Chen and Y. Peng, "Effect of annealing temperature on the structure and optical properties of sputtered TiO2 films," *J All. and Comp.,* vol. 509, pp. 4060-4064, 2011.

[74] V. Castrejón-Sánchez, E. Camps and M. Camacho-López, "Quantification of phase content in TiO2 thin films by Raman spectroscopy," *Superf. y vacio,* vol. 27, no. 3, pp. 88-92, 2014.

[75] N. Serpone, D. Lawless and R. Khairutdinov, "Size Effects on the Photophysical Properties of Colloidal Anatase Ti02 Particles: Size Quantization or Direct Transitions in This Indirect Semiconductor?," *J. Phys. Chem.,* vol. 99, pp. 16646-16654, 1995.

[76] M. Iliev, V. Hadjiev and A. Litvinchuk, "Raman and infrared spectra of brookite (TiO2): Experiment and theory," *Vib. Spec.,* vol. 64, pp. 148-152, 2013.

[77] T. I. Ji-Guang Li, "Brookite --> rutile phase transformation of TiO2 studied with," *Acta Mater.,* vol. 52, pp. 5143-5150, 2004.

[78] M. Iliev, V. Hadjiev and A. Litvinchuk, "Raman and infrared spectra of brookite (TiO2): Experiment and theory," vol. 64, pp. 148-152, 2013.

[79] M. T. Dove, Introduction to Lattice Dynamics, New York: Cambridge University Press, 1993.

[80] U. Rau, D. Abou-Ras and T. Kirchartz, Advanced characterization techniques for thin film solar cells, Weinheim, Germany: Wiley-VCH, 2011.

[81] S. Chung, Y. Kim, J. Kim and Y. Kim, "Multiphase transformation and Ostwald's rule of stages during crystallization of a metal phosphate," *Nature Phys.,* vol. 5, pp. 68-73, 2009.

[82] H. Wang and R. J. Composto, "Understanding morphology evolution and roughening in phase-separating thin-film polymer blends," *Europhys. Lett.,* vol. 50, no. 5, 2000.

[83] A. Mattsson and L. O. Sterlund, "Adsorption and Photoinduced Decomposition of Acetone and Acetic Acid on Anatase, Brookite, and Rutile TiO2 Nanoparticles," *J. Phys. Chem. C,* vol. 114, no. 33, p. 14121–14132, 2010.

[84] S. D. Ventura, E. G. Birgin, J. M. Martínez and I. Chambouleyrona, "Optimization techniques for the estimation of the thickness and the optical parameters of thin films using reflectance data," *J. App. Phys.,* vol. 97, p. 043512, 2005.

[85] J. Tauc, "Absorption Edge and Internal Electric Fields in Amorphous Semiconductors," *Mater. Res. Bull.,* vol. 5, pp. 721-730, 1970.

[86] B. D. Viezbicke, S. Patel, B. E. Davis and D. P. I. Birnie, "Evaluation of the Tauc method for optical absorption edge determination: ZnO thin films as a model system," *Phys. Stat. Soli. b,* vol. 252, no. 8, pp. 1700-1710, 2015.

[87] B. e. a. Sadigh, "First-Principles Calculations of the Urbach Tail in the Optical Absorption Spectra of Silica Glass," *Phys. Rev. Lett.,* vol. 106, p. 027401, 2011.

[88] L. V. R. Marcos and J. I. Larruquert, "Analytic optical-constant model derived from Tauc-Lorentz and Urbach tail," *Optics Express,* vol. 24, no. 25, p. 28561, 2016.

[89] M. N. Polyanskiy, "RefractiveIndex.INFO," [Online]. Available: https://refractiveindex.info. [Accessed 1 January 2017].

[90] Y. e. a. Hishikawa, "Interference-Free Determination of the Optical Absorption Coefficient and the Optical Gap of Amorphous Silicon Thin Films," *Jap. J. App. Phys.,* vol. 30, no. 5, pp. 1008-1014, 1991.

[91] M. Landmann, E. Rauls and W. G. Schmidt, "The electronic structure and optical response of rutile, anatase and brookite TiO2," *J, Phys.: Cond. Mater.,* vol. 24, 2012.

[92] Y. Luo, A. Benali, L. Shulenburger, J. T. Krogel, O. Heinonen and P. R. C. Kent, "Phase stability of tio 2 polymorphs from diffusion quantum monte carlo," *New J. Phys.,* vol. 18, no. 11, 2016.

APPENDICES

A1. Crystalline Depositions

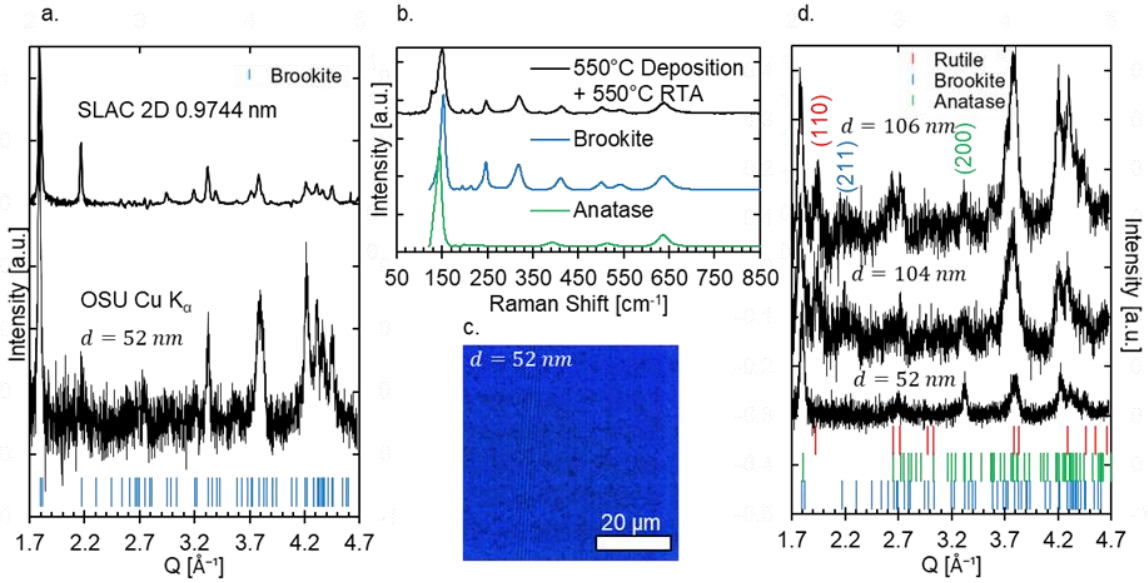

Figure A1: GIXRD and Raman spectroscopy of films deposited at 550°C with 1 mTorr of oxygen pressure on an SLS substrate. (a) Comparison of XRD from SLAC synchrotron data and OSU Cu K_α data collected on a 52 nm thick sample. (b) micro-Raman spectrum of film in (a) (black) with reference spectra for comparison with the RRUFF database, blue for brookite and green from anatase. (d) XRD spectra of a series of films deposited at 550°C with difference thicknesses (106 nm, 104 nm, and 52 nm) and deposition rates (0.14 Å/s, 0.21 Å/s. 0.07 Å/s).

While all the reports in the previous sections investigate the transitions from amorphous to crystalline transition it is possible to obtain similar results in films deposited at temperature. Figure A1 shows a series of samples, all deposited at 500°C with 1 mTorr oxygen pressure. Figure A1(c) shows the optical microscope image of one of the samples deposited at temperature that is distinctly lacking in the morphological variations observed in the post-anneal, amorphous depositions. However, as the SLAC XRD shows, the unique brookite (211) peak at 2.17 $Å^{-1}$ is clearly present though not easily identified within the Cu K_α spectrum. The Raman spectrum in Figure A1(b) confirms the presence of brookite for the sample in Figure A1(a). To determine the effects of thickness and deposition rate at temperature a few different thicknesses were tested using the same deposition conditions.

Figure A1(d) shows three different GIXRD spectra obtained using Cu K_α radiation. The thicker films show an increased contribution from the rutile structure as seen by the intensity of the rutile (110) peak at 1.91 $Å^{-1}$. However, without synchrotron data it is difficult to separate the contribution of the

anatase from that of the brookite structure definitively. For instance, there are two features on the 104 nm thick sample which indicate the presence of brookite, a shoulder on the main diffraction peak around 1.82 $Å^{-1}$ and a slight increase in the intensity of the (211) peak at 2.17 $Å^{-1}$. Unfortunately, both contributions are small within a dataset exhibiting a low signal to noise ratio and so are only suggestive and not conclusive. However, the data in Figure A1(a)-(c) does show that it is possible to produce more uniform brookite thin films at temperature. A more thorough examination of the effects of crystalline depositions is needed to explore the stability range of the brookite structure.

A2. Optical Band Gap Determination: Toy Model Approach

In researching the optical band gap for a TiO_2 a wide range of values and assumptions can be found, Table A1. For instance, while all theoretical evaluations for both anatase and brookite agree that the band gap transitions are indirect and direct respectively one can find examples in the literature where the incorrect assumption of gap type is assumed [67] [83]. In this section we conduct a review of some 129 experimental and theoretically reported values of the band gaps for the rutile, anatase, and brookite polymorphs, Table A1. We find that not only are there a wide array of values reported for the band gap energy of each polymorph but that even using the same process to determine band gap value the assumption can vary as well. For instance, the theoretical calculations for the band gap for both anatase and brookite agree that they are indirect and direct transitions respectively, but within the literature one can find instances where experimental evaluations of the band gaps assumed that anatase was direct and brookite indirect.

Table A1: Optical band gap values reported for the three major polymorphs of TiO_2. The average band gaps reported experimentally for the three polymorphs are on average consistent with those predicted theoretically. The average theoretical band gaps were determined from multiple reports of calculations performed using DFT-GW calculations with different functionals (PBE, HSE06) also correcting for excitonic effects using BSE.

Polymorph	Indirect Min eV	Indirect Max eV	Indirect Avg eV	Direct Min eV	Direct Max eV	Direct Avg eV
Rutile^{exp}	2.57	3.41	3.12	2.2	3.65	3.24
Rutileth	3.23	3.23	3.23	3.28	3.73	3.49
Anatase^{exp}	3.01	3.42	3.31	3.33	3.75	3.6
Anataseth	3.57	4.05	3.73			
Brookite^{exp}	3.24	3.57	3.32	3.22	3.79	3.41
Brookiteth				3.45	3.86	3.64

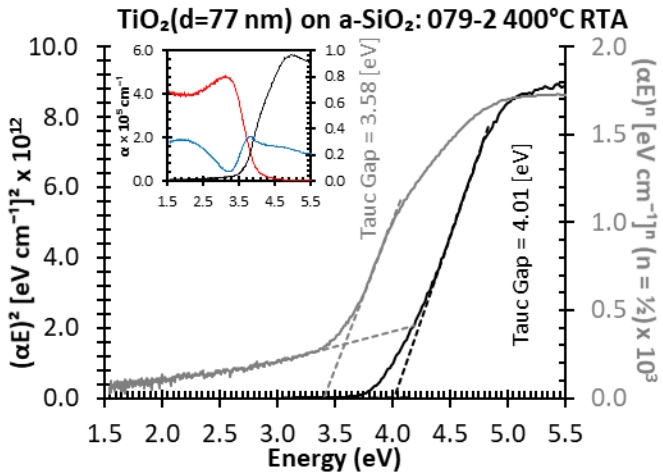

Figure A2: Tauc analysis including linear function to compensate for sub gap absorption effects on the band gap. The indirect gap analysis (applicable for the anatase structure of this film) suffers greatly from sub-bap absorption and extrapolating to the horizontal axis would result in a gap value of 3.4 eV. Incorporating the sub-gap absorption into the analysis results in a band gap value of 3.58 eV which is a bit high for anatase (most likely due to quantum effects related to the film thickness). The inset includes the transmission, reflection, and absorption plots over this same energy range.

To evaluate the errors associated with making an error in the assumption of gap type we use a toy model approach based on experiences from determining band gap energies for real films. First however, we should examine the process used to determine band gap energies in real films.

We begin the process of determining band gap energy by first determining the optical properties of our material, namely the absorption. The way in which the optical properties are determined is by the Pointwise Unconstrained Minimization Approach (PUMA) [84]. The parameters used in PUMA include the same approximation to the Sellmeier index of refraction as used in SCOUT, the film thickness, and the interference fringe positions.

Once the optical absorption spectrum is obtained, the optical band gap energy is determined by combining a Tauc analysis [85] [86] with an Urbach analysis [87] [88]. The Tauc analysis involves linearization of the onset of absorption ($\alpha E = A_T\left(E - E_g\right)^m$) by constructing the quantity $(\alpha E)^{1/m}$ where m is chosen as either 1/2 or 2 based on theoretical determination of the band gap type (1/2 for direct and 2 for indirect). The Urbach analysis models the sub-gap absorption, caused by disorder in the crystal, as an exponential decay ($\alpha = A_U e^{E/E_U}$) where A_U is a constant and E_U is the Urbach energy associated with the disorder in the crystal. An example of a material exhibiting both properties is shown in Figure A2. In combining these two descriptions of the optical absorption in a real crystal, the method used to determine the optical band gap includes first linearization of the absorption by constructing the Tauc plot; then, instead of extrapolating the linear region to the horizontal axis, the

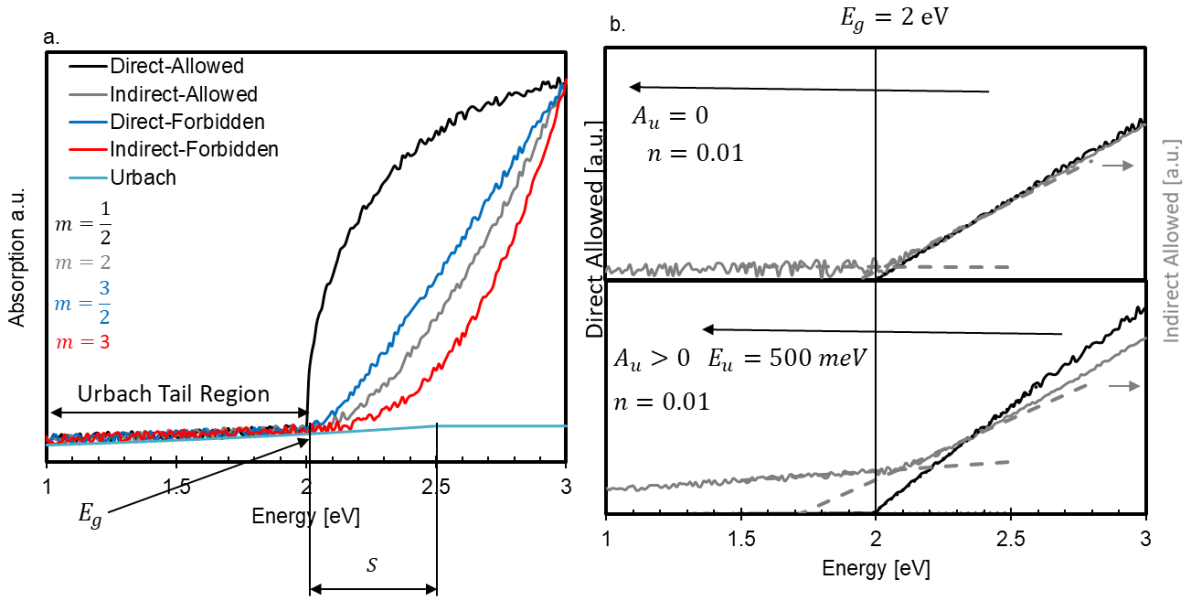

Figure A3: (a) Toy optical absorption model based Tauc optical absorption model. (b)Tauc analysis of the Toy model in (a) for both the direct and indirect gap models with and without Urbach energy and the affect it has on the linearization process used in the Tauc analysis.

intersection between the Tauc linear region and a linear function describing the Urbach tail states[4] is used to define the band gap energy. Now in the process of evaluating hundreds of films for band gap energies an automated procedure in Excel was developed to speed up the process and once developed was simple to extend to a toy model system with idealized parameters.

Based on the theoretical description of the absorption across the band gap the toy model was codded into Excel as,

$$\alpha(E) = \begin{cases} nA_u e^{\frac{E}{E_u}} & E < E_g + S \\ n\frac{A_T}{E}\left(E - E_g\right)^m + C & E \geq E_g \end{cases} \qquad (0\text{-}1)$$

where n is a random number between 0 and 1 simulating noise, A_u is the amplitude of the Urbach tail states, E_u is the Urbach energy, S is the overlap region between the band gap absorption and Urbach tail states, A_T is the amplitude of the onset of absorption, E_g is the band gap energy, m is the gap transition exponent (1/2 for direct-allowed, 2 for indirect-allowed, 3/2 for direct-forbidden, and 3 for indirect-forbidden), and C is a correction factor needed to make the piecewise absorption continuous. A visual description of the model parameters can be seen in Figure A3(a). An interesting

[4] From a comparison of Figure A2 and Figure A3(b) this appears to be a reasonable approximation

feature in the absorption related to the Urbach tail states that can be seen in Figure A3(b) is that while the Tauc plot for a direct-allowed optical transition is minimally affected, the Tauc plot for an indirect-allowed transition is significantly shifted.

To explore the effects of this shift on the determination of the band gap, for all four types of gaps the Tauc analysis was repeated for the three cases, clean data without Urbach characterization, noisy data with Urbach characterization, and noisy data without Urbach characterization. Figure A4 shows the results of the band gap energy determined for the three cases, for all four band gap types, all of which were analyzed with each of the four gap assumptions. In Figure A4 the back bars throughout the bar chart correspond to the specific band gap type analyzed using the correct assumption (e.g. indirect-allowed analyzed as indirect-allowed). One of the most striking features seen in Figure A4 is that of all the band gap types, the direct-allowed transition appears to be the most sensitive to incorrect assumptions. However, of all the transition types the direct-allowed shows the least deviation when analyzed with the correct assumption even with noisy data and Urbach tail states. Whereas, as soon as noise or Urbach energy is added into the system all other band gap show

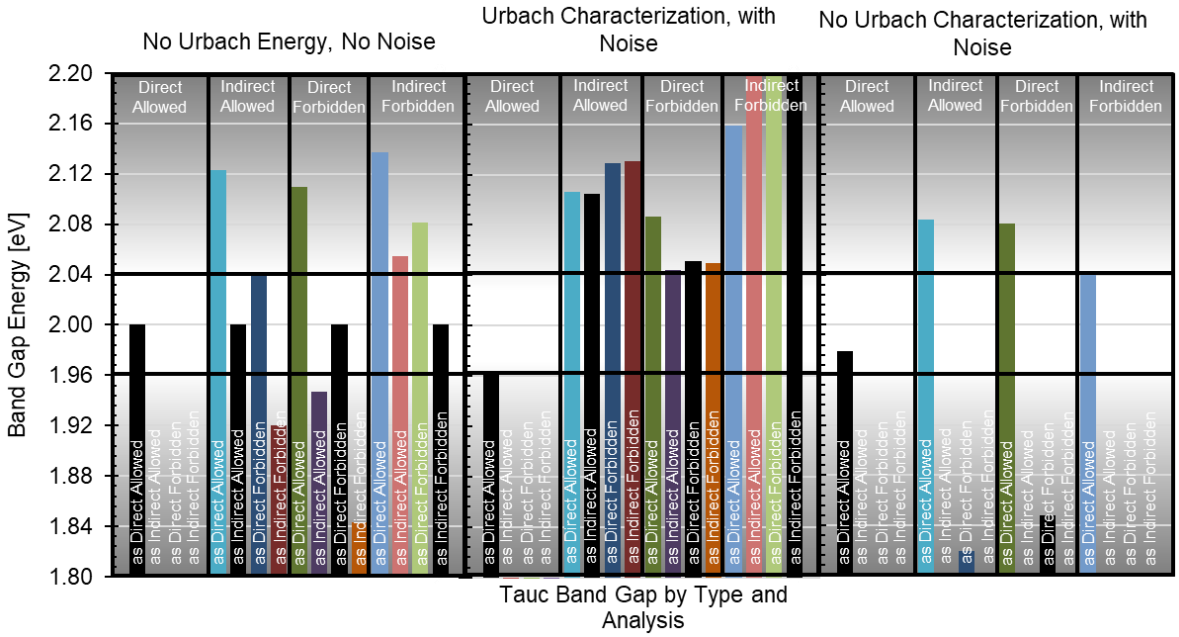

Figure A4: Toy model analysis for the three cases from left to right, without Urbach energy and without noise, Urbach energy with characterization with noise, Urbach energy without characterization with noise. Black bars correspond to the analysis performed on the correct spectrum such as a direct spectrum analyzed assuming direct transition, while the colored bars correspond to assuming an incorrect transition for analysis.

deviation greater than 5% from the correct value and without compensation for the Urbach tail states most of the band gap types deviation more than 20% from the correct value.